

## ANALYZING STAR CLUSTER POPULATIONS WITH STOCHASTIC MODELS: THE *HUBBLE SPACE TELESCOPE*/WIDE FIELD CAMERA 3 SAMPLE OF CLUSTERS IN M83

MORGAN FOUESNEAU<sup>1,2</sup>, ARIANE LANÇON<sup>1</sup>, RUPALI CHANDAR<sup>3</sup>, AND BRADLEY C. WHITMORE<sup>4</sup>

<sup>1</sup> Observatoire astronomique et CNRS UMR 7550, Université de Strasbourg, Strasbourg, France; morgan.fouesneau@astro.u-strasbg.fr

<sup>2</sup> Department of Astronomy, University of Washington, Seattle, WA, USA

<sup>3</sup> Department of Physics and Astronomy, University of Toledo, Toledo, OH, USA

<sup>4</sup> Space Telescope Science Institute, Baltimore, MD, USA

Received 2011 July 29; accepted 2012 February 14; published 2012 April 16

### ABSTRACT

The majority of clusters in the universe have masses well below  $10^5 M_{\odot}$ . Hence, their integrated fluxes and colors can be affected by the presence or absence of a few bright stars introduced by stochastic sampling of the stellar mass function. Specific methods are being developed to extend the analysis of cluster energy distributions into the low-mass regime. In this paper, we apply such a method to real observations of star clusters, in the nearby spiral galaxy M83. We reassess the ages and masses of a sample of 1242 clusters for which  $UBVIH\alpha$  fluxes were obtained from observations with the Wide Field Camera 3 instrument on board the *Hubble Space Telescope*. Synthetic clusters with known properties are used to characterize the limitations of the method (valid range and resolution in age and mass, method artifacts). The ensemble of color predictions of the discrete cluster models are in good agreement with the distribution of observed colors. We emphasize the important role of the  $H\alpha$  data in the assessment of the fraction of young objects, particularly in breaking the age-extinction degeneracy that hampers an analysis based on  $UBVI$  data only. We find the mass distribution of the cluster sample to follow a power law of index  $-2.1 \pm 0.2$ , and the distribution of ages a power law of index  $-1.0 \pm 0.2$  for  $\log(M/M_{\odot}) > 3.5$ , and ages between  $10^7$  and  $10^9$  yr. An extension of our main method, which makes full use of the probability distributions of age and mass obtained for the individual clusters of the sample, is explored. It produces similar power-law slopes and will deserve further investigation. Although the properties derived for individual clusters significantly differ from those obtained with traditional, non-stochastic models in about 30% of the objects, the first-order aspect of the age and mass distributions is similar to those obtained previously for this M83 sample in the range of overlap of the studies. We extend the power-law description to lower masses with better mass and age resolution and without most of the artifacts produced by the classical method.

**Key words:** galaxies: individual (M83) – galaxies: star clusters: general – methods: data analysis – methods: statistical – techniques: photometric

*Online-only material:* color figures

### 1. INTRODUCTION

Many and possibly most stars form in clusters rather than individually. Much observational effort has therefore been invested to determine the distributions of star cluster ages and masses (Searle et al. 1980; Larsen & Richtler 2000; Billett et al. 2002; Hunter et al. 2003; Fall et al. 2005; Dowell et al. 2008; de Grijs 2009; Larsen 2009; Chandar et al. 2010; Bastian et al. 2011), and to determine the dominant mechanisms of cluster formation and disruption (Kroupa & Boily 2002; Lamers et al. 2005; Whitmore et al. 2007; Parmentier & de Grijs 2008; Fall et al. 2009; Elmegreen & Hunter 2010; Converse & Stahler 2011). With the *Hubble Space Telescope* (*HST*) and especially its latest survey instrument Wide Field Camera 3 (WFC3), cluster samples have been detected in external galaxies down to a regime in which cluster luminosities overlap those of individual bright stars, and hence to lower masses (Johnson et al. 2011). Because cluster luminosity (and mass) distributions rise steeply toward lower luminosities (and masses), these deeper surveys have led to significantly larger cluster samples.

In the low-mass regime, clusters of a given age and mass are predicted to display a broad range of integrated luminosities and colors, mostly as a consequence of the random sampling of the upper part of the stellar mass function (Barbaro & Bertelli 1977; Girardi & Bica 1993; Lançon & Mouhcine 2000; Bruzual

2002; Cerviño & Luridiana 2006; Deveikis et al. 2008). For the sake of simplicity, we will refer to stellar population model implementations that explicitly predict luminosity and color distributions as *stochastic models*. The predicted distributions depend in non-trivial ways on the cluster mass. Stochastic models are usually based on Monte Carlo simulations, although first attempts at analytical approaches have been made (Cerviño & Luridiana 2006). Traditionally, stellar population models have been implemented with the assumption of a fully sampled stellar initial mass function (IMF): each stellar mass bin along an isochrone contains exactly the mass fraction prescribed by the IMF, regardless of the fact that this may lead to unphysical non-integer numbers of stars in some of the most luminous phases of evolution. These implementations, which we will refer to as *continuous models*, do not predict distributions of cluster luminosities and colors but rather their mean values (and sometimes their first moments).

Monte Carlo simulations of low-mass clusters have shown that the range of broadband colors predicted with this type of stochastic model are in rather good agreement with observed ones in the Milky Way and in the Magellanic Clouds (Girardi & Bica 1993; Piskunov et al. 2009; Popescu & Hanson 2010). The color and luminosity distributions are complex in the low-mass regime. They display multiple peaks. The most probable luminosities and colors differ from the mean color

of the distribution, and conversely the mean properties are unlikely to occur in any actual cluster. Therefore, ages and masses derived from the analysis of cluster luminosities and colors are expected to depend on the type of model used (i.e., stochastic or continuous). For different combinations of broadband filters, Maíz Apellániz (2009) and Fouesneau & Lançon (2010) confirmed that the analysis of the integrated light of *synthetic* low-mass clusters with *continuous* models leads to biases in the assignment of ages to individual objects.

Assigning fundamental properties to individual clusters and studying the global properties of the cluster population of a galaxy are two different issues. For instance, Fouesneau & Lançon (2010) showed that the mass estimates determined for low-mass clusters with continuous models would be dispersed around the real values, but that there would not be a strong global impact on the cluster mass distribution itself. This work also indicated that high-resolution features in the cluster age distribution would be affected, but Fouesneau & Lançon (2010) did not examine whether any of these biases would be strong enough to modify the global, low-resolution age distribution of a typical cluster sample.

The main purpose of the article of Fouesneau & Lançon (2010) was to introduce two analysis methods for the interpretation of integrated fluxes of low-mass star clusters, both based on a large collection of Monte Carlo simulations of clusters of finite numbers of stars, i.e., on stochastic models. One analysis method is a traditional  $\chi^2$  minimization. The second one rests on the calculation of posterior probability distributions in age–mass–extinction space. The latter refers explicitly to Bayes’ theorem, in which the posterior probabilities of model parameters given a set of data are expressed in terms of their prior distributions and of the probability distributions of observational errors. Although the results from the analysis methods have their own model dependencies through the adopted population synthesis code and the priors, it is clearly a conceptual improvement to move away from the restricted framework of continuous population synthesis models. Studies in the regime well below  $10^4 M_\odot$ , where the literature on the subject does not usually venture, become possible. This should allow us to examine cluster formation and disruption histories in more detail in the future.

In this paper, we apply the methods of Fouesneau & Lançon (2010) to the WFC3 sample of star clusters in M83 first presented by Chandar et al. (2010). Messier 83, the “Southern Pinwheel” galaxy, is one of the best nearby analogs of the Milky Way. These data allow us to compare standard age and mass estimates based on continuous models with those based on stochastic ones for a sample of *real* objects. We also investigate how the use of stochastic models affects the age and mass distributions of the sample as a whole.

The rest of this paper is organized as follows. Section 2 summarizes the data, cluster selection, and photometry, and Section 3 summarizes and extends predictions from the stochastic models developed by Fouesneau & Lançon (2010). Section 4 compares the luminosity and color distributions of the colors and model predictions. Expectations from artificial clusters are presented in Section 5, and results for real clusters in M83 are presented in Section 6. Section 7 discusses several key issues, including the importance of using a narrowband filter in the analysis, and a direct comparison of results from stochastic and continuous models. More details relevant to this comparison are provided in two appendices. Section 7 also presents preliminary exploration of an alternative determination of the age–mass

distribution of the cluster sample of M83, one which uses the probability distributions of individual clusters rather than just their most probable values. Section 8 presents the main conclusions of our work.

## 2. DATA AND OBSERVATIONS

In order to take advantage of the wavelength coverage of WFC3, images of M83 were taken as part of ERS1 program 11360 (PI: O’Connell) through seven broadband filters from the UV to the near-infrared: F225W (*UV*), F336W (*U*), F438W (*B*), F555W (*V*), F814W (*I*), F110W (*J*), and F160W (*H*). They cover the nucleus and the northeastern part of the galaxy. The color image in Figure 1 illustrates the observed region. In addition, narrowband filter observations were taken for the following emission lines: [O III] (F373N), H $\beta$  (F487N), O II (F502N), H $\alpha$  + [N II] (F657N), and [S II] (F673N).

In this paper, we focus only on the broadband *UBVI* photometry (*HST*/WFC3 passbands) and the narrowband H $\alpha$  measurements (F657N). The sample contains 1242 star clusters with measurements in these five bands.<sup>5</sup> They were selected based on a “white” light image (i.e., a co-added, rms-normalized combination of the *U*, *B*, *V*, and *I* filters), in order to give roughly equal weight to all wavelengths. A combination of size and concentration criteria measured in the *V* band was used to separate individual stars from clusters, as described in Chandar et al. (2010). For each object, circular aperture photometry with an aperture radius of 3 pixels ( $0.^{\prime\prime}0396 \text{ pixel}^{-1}$ ) produced integrated flux values which were then corrected for foreground galactic extinction (Schlegel et al. 1998; Appendix B). Measurement uncertainties are typically spread between 0.05 and 0.25 mag for the *B*, *V*, and *I* broad bands (cf. Section 5). About one half of the objects have uncertainties larger than 0.25 in the *U* and H $\alpha$  filters. The average errors increase nonlinearly with magnitude. Instrumental magnitudes were converted into the Vega magnitude system by applying the following zero points: F336W = 23.46, F438W = 24.98, F555W = 25.81, F814W = 24.67, and F657N = 22.35. We assume a distance of 4.5 Mpc to M83 as found in Thim et al. (2003), which corresponds to a distance modulus of  $m - M = 28.29$ .

## 3. POPULATION SYNTHESIS MODELS

We aim at studying the age–mass distribution of the clusters in M83, using the method of Fouesneau & Lançon (2010). The method is based on a large collection of Monte Carlo simulations of individual clusters. The synthetic clusters are constructed with the population synthesis code PÉGASE.2N (M. Fouesneau et al. 2012, in preparation), which is derived from PÉGASE (Fioc & Rocca-Volmerange 1997). As in the original (continuous) population synthesis code, the underlying stellar evolution tracks are those of the Padova group (Bressan et al. 1993), with a simple extension through the thermally pulsating asymptotic giant branch based on the prescriptions of Groenewegen & de Jong (1993). The input stellar spectra are taken from the library of Lejeune et al. (1997). The stellar IMF is taken from Kroupa et al. (1993) and extends from 0.1 to  $120 M_\odot$ . Nebular emission (lines and continuum) is included in the calculated spectra and broadband fluxes under the assumption that no ionizing photon escapes. Line ratios are computed as in Fioc & Rocca-Volmerange (1997). When extinction corrections are

<sup>5</sup> The cluster catalog, including photometry and positions, can be retrieved at <http://archive.stsci.edu/prepds/wfc3ers>.

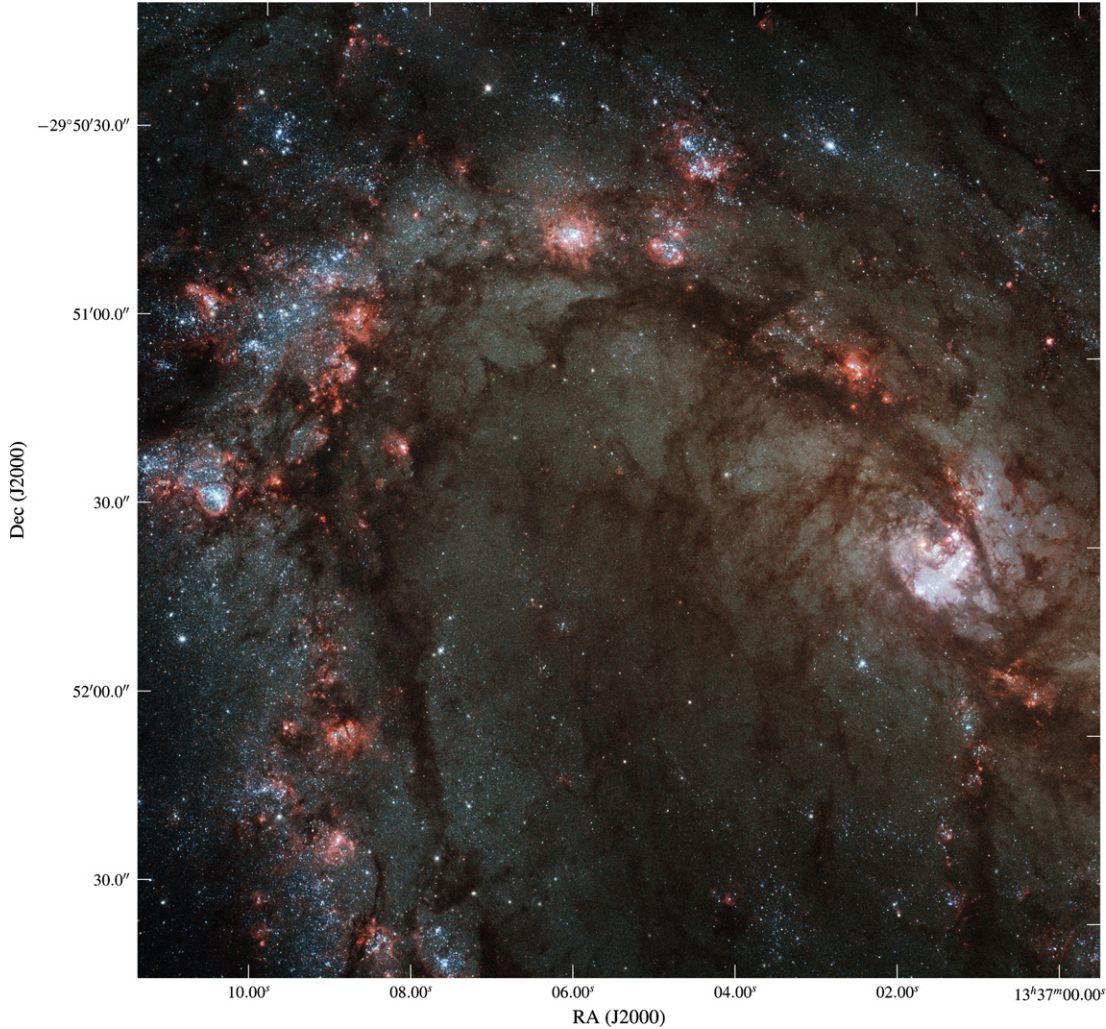


**Figure 1.** Color image of the observed region of M83 with the WFC3 instrument on board *HST*. The *B*-band (F438W) image is shown in blue, the *V*-band (F555W) image in green, and a combination of the *I* band (F814W) and  $H\alpha$  in red. The covered area represents  $2.75 \times 2.75 (\approx 3.6 \times 3.6 \text{ kpc}^2)$ .

considered, they are based on the standard law of Cardelli et al. (1989). The synthetic photometry for the artificial clusters is computed using the response curves of the *HST*/WFC3 filters. A reference spectrum of Vega provides zero magnitude fluxes (Bohlin 2007).

In the context of studying M83, the model collection is restricted to solar metallicity, the metallicity of this galaxy according to Gil de Paz et al. (2007). The simulated cluster set has been extended to higher masses than available in Fouesneau & Lançon (2010), and now covers masses from  $10^3$  to  $5 \times 10^5 M_\odot$  and ages from 1 Myr to 20 Gyr. With  $1.4 \times 10^7$  individual objects, the collection is large enough to include all reasonably likely cluster properties. The ages of the synthetic clusters are drawn from a power-law distribution with index  $-1$  (equal numbers of star clusters per logarithmic age bin), rounded to integer multiples of  $10^6$  yr. For practical reasons (the need to include more massive clusters without having to recompute prohibitive numbers of low-mass clusters), the mass distribution in the new collection of models also follows a power law of index  $-1$ , instead of the previously adopted  $-2$  in Fouesneau & Lançon (2010).<sup>6</sup>

<sup>6</sup> The number of massive clusters in the current collection is larger than strictly necessary. The choice of the power-law index can be optimized in the future to construct smaller representative cluster sets.

The age and mass distributions of the synthetic clusters, together with the values allowed for extinction, are the main assumptions (priors) of the inversion. These distributions account for two major qualitative trends found in star-forming galaxies: low-mass clusters are more numerous than high-mass clusters, and, because of a variety of efficient disruption mechanisms, young clusters are more numerous than old ones. In the future, it will be interesting to implement an iterative inversion, in which the derived cluster age and mass distributions, corrected for selection effects, are re-injected as priors until the procedure converges.

#### 4. LUMINOSITY AND COLOR DISTRIBUTIONS

Previous work by Chandar et al. (2010) shows that the *V*-band luminosity function of the observed clusters can be described globally as a power law with index  $\sim -2$  down to the completeness limit located near  $M_V = -5$ . For the four other bands used here, the turnover points in the luminosity distributions are located near  $M_U = -6$ ,  $M_B = -5$ ,  $M_I = -6$ , and  $M_{H\alpha} = -6$  (in the absolute Vega magnitude system). For brevity, we will refer to these turnover points as “completeness limits.” Note that Chandar et al. (2010) estimated that this cluster catalog contains contamination at the approximately

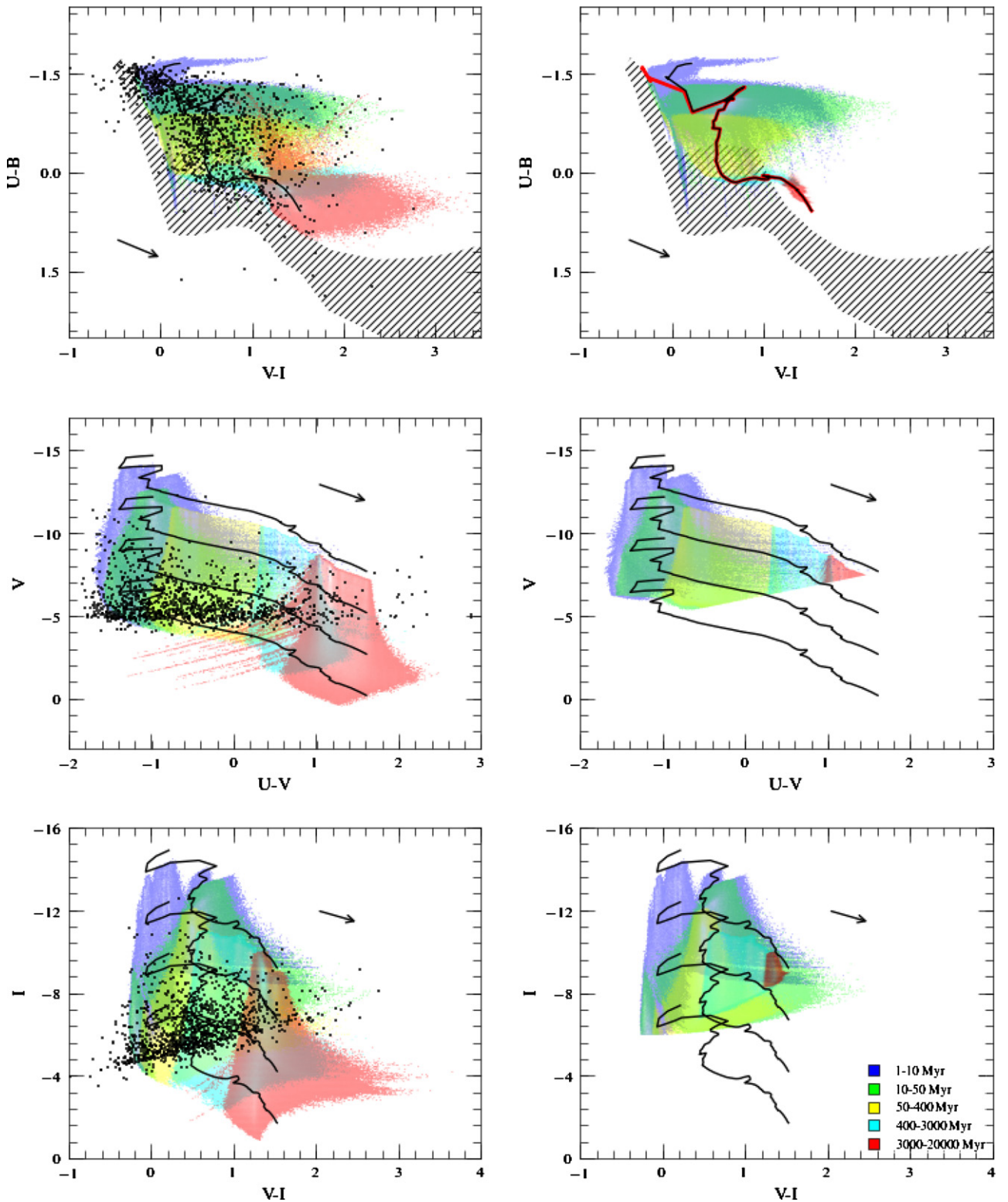


**Figure 2.** Color–color and color–magnitude diagrams of the observed clusters (black points) and the models. Magnitudes are in the Vega system, in the WFC3 filters. Solid lines show the predictions obtained with the corresponding “continuous” population synthesis models for  $10^3$ ,  $10^4$ ,  $10^5$ , and  $10^6 M_{\odot}$ . The red line in the top right panel shows the effect of excluding any ionized gas emission from the predicted fluxes. Colored dots represent the discrete clusters available in the Monte Carlo collection. The color code is given in the bottom right panel. In the right-hand panels, only discrete models brighter than the observational limits in  $UBVI+H\alpha$  are shown. Models are not reddened in any panel, but the extinction vector for  $A_V = 1$  is shown. Hatched regions represent the expected colors of individual stars.

15% level from individual stars in crowded regions and from chance superpositions of a few stars.

Figure 2 compares the loci of the observations and the models in three projections of color–magnitude space. In the left-hand

panels, the data are shown together with the complete set of models, which will be used to assign age, mass, and extinction estimates to each individual object. The majority of the observed clusters lie well within the regions covered by the synthetic

clusters. It is also clear that some of the observations cannot be reproduced with continuous population synthesis models, even when allowing for extinction. The clusters with the bluest ( $V - I$ ) colors are those whose post-main sequence happens to be underpopulated, while the clusters with the reddest ( $V - I$ ) colors may either happen to have more luminous red stars than average, or be severely reddened (or both).

At very young ages, the color predictions are sensitive to the prescription adopted for the nebular emission: the nebular fluxes added to the stellar fluxes produce redder WFC3  $V - I$  colors (to allow comparison, the red line in Figure 2 illustrates the effect of discarding the gas contribution, in the case of continuous models). This leads to the hook-like extension seen in blue at the top of the upper panel of Figure 2, composed of low-mass clusters (a few  $10^3 M_{\odot}$ ) with a number of ionizing stars in excess of the average. They do not have counterparts in the observed cluster sample. The models in that part of the diagram represent only 0.1% of the models with ages below 3 Myr, and will therefore have little effect on any of our results. On the other hand, the very blue colors observed for a subset of obviously young clusters in M83 suggest that the nebular emission included in our models is too high for some objects; this could affect age-dating, mainly between 1 and 4 Myr.

One can conclude from the two bottom left panels of Figure 2 that a majority of the observed clusters have masses lower than  $10^4 M_{\odot}$ . At these masses, the predicted optical fluxes of star clusters are spread quite widely. For instance, the 90% confidence intervals for the predicted fluxes, respectively, have widths of 0.3 dex at 5 Myr in the  $V$  band, 0.1 dex at 50 Myr in  $V$ , and 0.5 dex at 5 Myr in the  $H\alpha$  filter (based on our Monte Carlo simulations). The distributions have complex shapes. This is the mass regime where the use of the method of Fouesneau & Lançon (2010) may be expected to produce the most significant changes with respect to traditional approaches. A main purpose of this paper is to illustrate to what extent this does (or does not) modify results for individual clusters and for the sample as a whole.

The right-hand panels illustrate some of the complex effects of magnitude limits. The models shown are those brighter than the “completeness limits” of the observations in all five bands. Some clusters are observed below these limits, because the luminosity distributions of the observations do not fall off abruptly beyond their turnover: 10% of the clusters are below the turnover of the luminosity function in  $V$  or  $H\alpha$ , 30%–40% in  $U$ ,  $B$ , and  $I$ . More complex figures are obtained when reddened models are included (not shown). In the stochastic context, a magnitude cut does not simply reject *all* the clusters of a given mass that have reached a critical age. On the contrary, the mass-to-light ratios in this regime have a large range of possible values. At a given mass and age only those stochastic clusters that happen to be fainter than the magnitude limits will be rejected, while those that happen to be brighter will be kept. From the figures shown here one should remember that the effects of a stochastically sampled IMF will be more important for the subset of young clusters than for the old ones, because the latter must be of high mass to be detected.

The model distributions are not and should not be truncated in magnitude when used to assign fundamental properties to individual clusters. The presence of low-luminosity clusters in the Monte Carlo sample can do no harm in the analysis of a cluster observation. On the other hand, the empirical sample may contain a small number of clusters with intrinsic luminosities below the “completeness limits” that made it into the sample

only thanks to favorable error bars. With a truncated theoretical distribution, the analysis would fail to provide correct properties for such objects.

In the future, however, it will be worthwhile to construct more sophisticated versions of the truncated model distributions in the right-hand panels of Figure 2. If the original Monte Carlo collection can be modified to account for all observational effects present in the M83 sample, the resulting synthetic color–magnitude distributions can be compared directly with the observed ones. This approach would be a direct analog of what has slowly become common practice in the analysis of the resolved *stellar* color–magnitude diagrams of nearby galaxies. In the latter case, the aim is to determine star formation histories. In our case current age–mass distributions could be estimated, without the detour through the individual analysis of each observed cluster. We have not yet implemented the tools necessary for such a study. The observational effects relevant to a cluster sample are more complex than those one deals within star samples (i.e., variable cluster surface brightness, size, effect of crowding, background fluctuations . . .). Correcting for them lies beyond the scope of this paper, and we will rather restrict conclusions about the cluster population of M83 to ranges where incompleteness is not severe.

## 5. EXPECTATIONS FROM ARTIFICIAL DATA

Fouesneau & Lançon (2010) assessed the methods used here to estimate cluster ages and masses. Using standard *UBVI* or *UBVIK* photometry and accounting for observational errors of 5% on the fluxes, they showed that it was possible to determine age distributions with a resolution in age much narrower than in non-stochastic studies. In this section, we briefly describe the behavior of the analysis when using photometry in the *UBVI* and  $H\alpha$  filters of *HST/WFC3*, with error bars distributed as in the actual M83 cluster data (Figure 3). Most of these uncertainties are larger than 5%. This experiment allows us to identify potential artifacts, and to determine what resolution in age to aim for in the analysis of the empirical data set. Unless otherwise stated, the second method of Fouesneau & Lançon (2010) is used in the analysis here and in subsequent sections, i.e., we maximize posterior probabilities. We refer to Section 7.4 for a discussion of a more complete exploitation of the posterior probability distributions.

The sample of synthetic clusters used as a mock data set contains 1000 objects and is built as follows: (1) the number of stars in each cluster is drawn from a power-law distribution with index  $-2$ , between  $10^3$  and  $10^6$  (which corresponds roughly to masses between  $500$  and  $5 \times 10^5 M_{\odot}$ ), (2) the logarithms of the cluster ages are drawn from a uniform distribution, (3) the uncertainties are assigned randomly to uncertainties taken from the list of clusters observed in M83 (see Figure 3), and (4) extinction is added with  $A_V$  distributed uniformly between 0 and 3. Note that no noise is added to the synthetic fluxes (the uncertainties assigned are used only in the inversion). As in Fouesneau & Lançon (2010), the physical quantities used in the inversion are fluxes, not magnitudes or colors. Errors initially provided in magnitudes are reinterpreted as symmetric errors on the fluxes.

The top panel of Figure 4 illustrates the input sample of synthetic clusters. The color scale refers to the continuum-subtracted  $H\alpha$  emission of the models,<sup>7</sup> which is directly related

<sup>7</sup> The continuum subtraction is performed for this illustration only; total narrowband fluxes are used in the analysis.

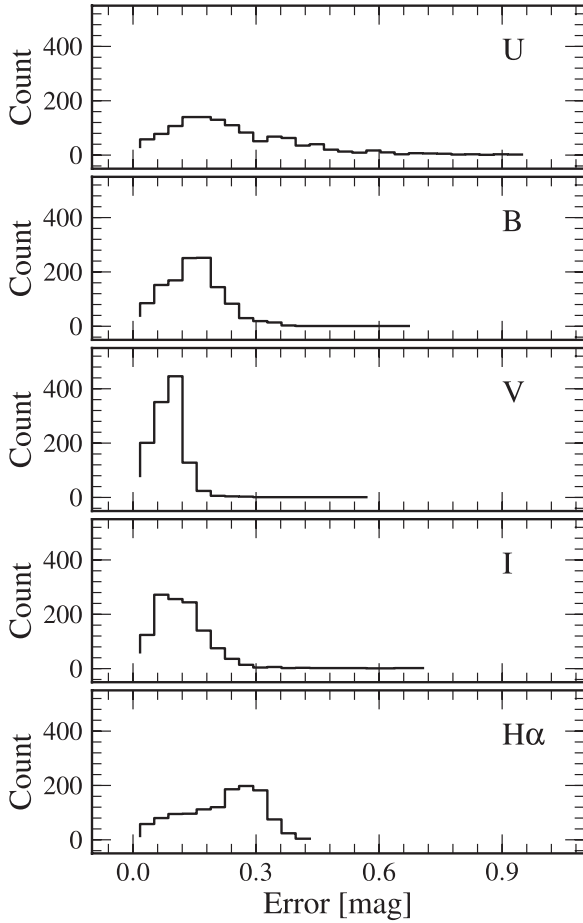


**Figure 3.** Photometric uncertainty distributions for the 1243 M83 cluster fluxes in the five photometric bands used in this study.

to the temperatures and luminosities of the hot bright stars. This  $H\alpha$  emission is significant only for clusters younger than 8 Myr (but some young clusters show none as they happen to contain no ionizing star). Note that unlike Figure 2, the synthetic clusters shown in Figure 4 are reddened, hence they trail down the reddening vector along diagonal lines. There is a region of overlap in broadband colors between models with and without  $H\alpha$  emission (i.e., the dark red points which represent clusters with no  $H\alpha$  emission overlap with the points of other colors which do emit  $H\alpha$ ). Including F657N data is expected to provide critical information in this regime.

The second and third panels of Figure 4 show that ages are recovered without large biases and that errors in the derived  $\log(A/\text{yr})$  have a quasi-normal distribution with a standard deviation of 0.14 dex (the global offset of 0.011 dex is not significant, it can be explained by a handful of outliers). Considering the substructure seen in the middle panel, we will not attempt to interpret features narrower than about 0.33 dex (FWHM of a Gaussian fit) in the age distributions obtained for the clusters of M83. The equivalent figures for the input and output masses show a dispersion of about 0.1 dex.

Large errors in age occur for a few percent of the synthetic clusters, and mostly at ages of one or a few Gyr. The origin of these is explained in Fouesneau & Lançon (2010, their Figures 5, 6, and 8). Regions of high model density in color–color space act as attractors in our analysis. If the locus of dereddened versions of the photometry of a cluster approaches such a densely populated region, the predominant age–mass

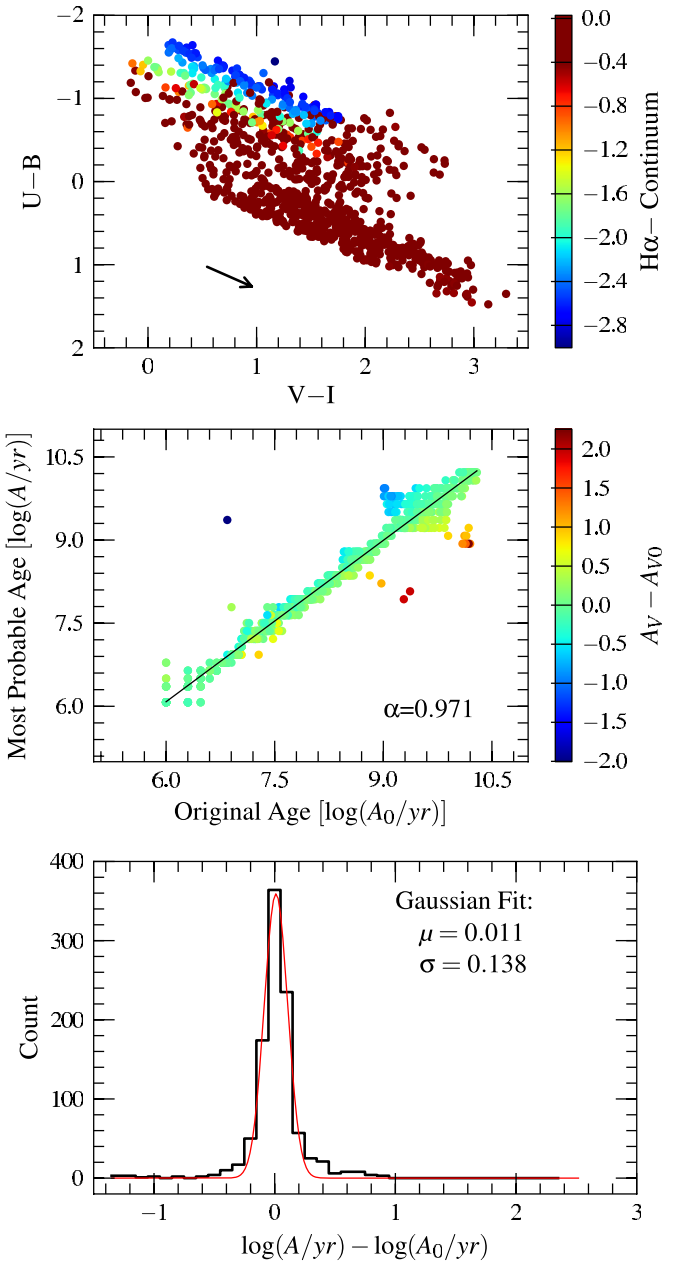


**Figure 4.** Analysis of the colors of the mock data (Section 5). Top: input sample. Colors highlight synthetic clusters with  $H\alpha$  line emission. Middle and bottom: comparison between input ages and derived ages. The linear regression shown has a slope of 0.971.

properties of the models located there will be considered most probable. If the cluster observed is in fact reddening-free, the result will be an overestimated extinction together with an underestimated age (the well-known age–extinction degeneracy is also present in the stochastic context). If the observed cluster is truly reddened, it sometimes happens that the analysis underestimates extinction and therefore overestimates age. This last situation, however, is unlikely to occur above 1 Gyr in the M83 sample, because most old reddened clusters are below our detection limit. A small percentage of young reddened clusters could be affected.

## 6. M83 CLUSTER AGES AND MASSES

We can now go back to M83 and estimate age, mass, and extinction for each of the clusters in the sample in the

stochastic context. As in Fouesneau & Lançon (2010), the assigned estimates are the age–mass–extinction triplets that maximize posterior probability, i.e., maximize the probability of the observed set of fluxes, given the underlying age and mass distributions of the model collection. The prior distribution in  $\log(\text{age})$  is uniform, the prior distribution in  $\log(\text{mass})$  is also uniform, the metallicity is solar, and  $A_V$  is allowed to take any value between 0 and 3 in steps of 0.2. We recall that the completeness limits of the observations are not used in any manner during the determination of individual ages and masses. A discussion of the errors on the estimates as derived from posterior probability distributions in age–mass space can be found in Section 7.4.

The age–mass–extinction distributions resulting from the analysis are shown in Figure 5. Derived masses range from the low limit of our model catalog ( $10^3 M_\odot$ ) to about  $5 \times 10^5 M_\odot$ . Ages are distributed between a few Myr and about 1 Gyr, with only a few candidates for ages older than 1 Gyr. The relative lack of old clusters was expected from the detection limits (Section 4). The middle panel of Figure 5 shows that very young clusters come with a large range of extinction values, as seen in many star-forming galaxies (e.g., Whitmore & Zhang 2002; H. Kim et al. 2012, in preparation). At ages older than  $10^7$  yr, clusters with more than 1 mag of extinction become rare. Between  $10^7$  and  $10^8$  yr, this most likely reflects a real lack of highly reddened objects, as the data’s detection limits in principle allow us to detect  $3 \times 10^7$  yr old clusters with masses above  $\log(M) \sim 3.7$  and up to 2 mag of extinction. At old ages, we do not expect many highly reddened clusters to be present in the disk of M83. But even if they existed they would have faded below the detection limits of the sample unless they were very massive.

The bottom panel is consistent with expectations again: at a given age, the upper envelope of the derived extinctions decreases with decreasing mass.

### 6.1. Cluster Ages

The distribution of all the cluster ages is shown in Figure 6. The age distribution of the clusters can be approximated by a power law, with an index  $-0.93 \pm 0.10$  for clusters more massive than  $\log(M/M_\odot) = 3.5$  and with ages between  $\approx 10^7$  and  $10^9$  yr. If we fit from  $3 \times 10^6$  to  $10^9$  yr instead, we find a power-law index of  $-1.12 \pm 0.18$ . The slope remains similar if we restrict the sample to even higher masses. These results are similar to those found by Chandar et al. (2010), although they used different ranges of masses and significantly broader bins to account for age-dating artifacts resulting from continuous models.

For ages between  $10^7$  and  $10^9$  yr, the sample’s age distribution is roughly flat in logarithmic age bins (top panel). Substructures are observed in some age distributions with different bin sizes and locations. These substructures disappear when the age distribution is plotted with bins wider than 0.4 dex. The distribution drops off at ages older than  $10^9$  yr, as expected from the observational selection limits.

The age distribution of the full sample has a peak at ages of  $(3\text{--}10) \times 10^6$  yr. The excess of clusters found at young ages, compared to a power-law extrapolation of the distribution at older ages, consists of low-mass objects ( $\log(M/M_\odot) < 3.5$ ). Objects with masses this small typically have faded below our detection limits when older than  $10^7$  yr. Imposing a mass cut at  $\log(M/M_\odot) = 3.5$  largely removes this peak.

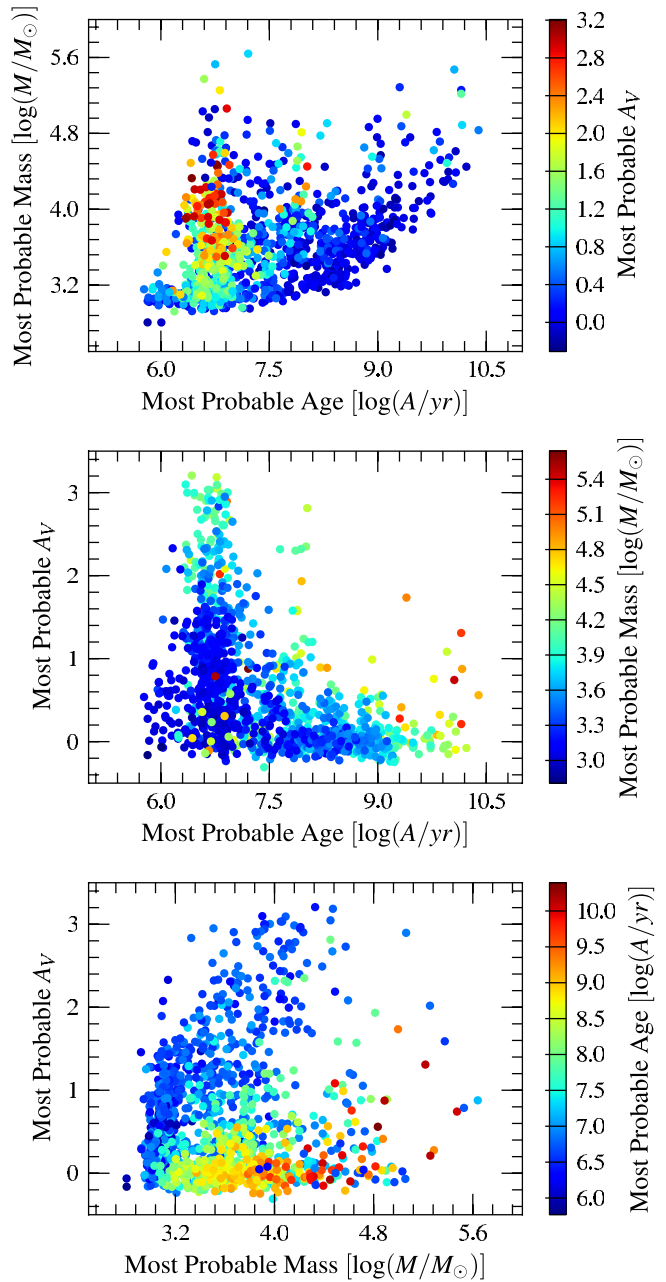


**Figure 5.** Age–mass–extinction distribution obtained with the method of Fouesneau & Lançon (2010). Noise is added to the dot positions along the different directions to reduce the overlap introduced by the binning method. A dispersion of 0.15 dex in age is used for this purpose, which corresponds to the minimal resolution determined in Section 5. A dispersion of 0.05 dex is used in mass and 0.1 in  $A_V$ . Colors refer to the third estimated parameter, according to the scale on the right-hand side.

Systematic errors are likely to affect the strength, width, and position of the peak at young ages. Indeed, the derived distribution falls to nearly zero below ages of about 3 Myr, despite the fact that M83 is still in the process of forming stars and clusters. It is likely that some of the clusters with estimated ages near 5 Myr are in fact younger. Reasons for possible systematics in this age range include: (1) the sensitivity of the age-dating to the assumed escape fraction of ionizing photons from the region in which the fluxes are measured (as discussed in Section 4), (2) some level of inconsistency between the stellar evolution models and the clusters in M83, (3) the fact that our current model collection contains only models with

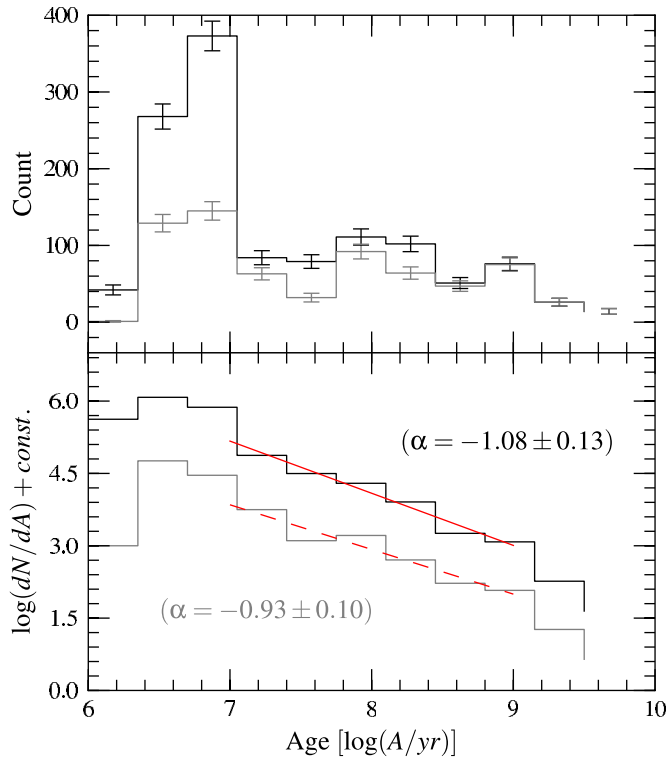


**Figure 6.** Age distribution obtained based on discrete population models. The top panel shows the  $dN/d \log(A)$  distribution whereas the bottom one shows the  $\log(dN/dA)$  distribution, which are the two commonly used representations in the literature. The black histograms represent the distribution for the whole set of detected clusters, whereas the gray ones only include objects with estimated masses above  $10^{3.5} M_{\odot}$ . Error bars are the Poisson noise dispersions in each bin. Solid and dashed lines represent power-law fits to the distributions of the bottom panels (for  $\log(A/\text{yr})$  between 7.0 and 9.0). The bin width is of 0.35 dex.

ages that are integer multiples of 1 Myr, (4) the lower-mass limit of the current collection, and (5) our restriction to  $A_V < 3$  in the analysis of cluster colors. A full usage of the posterior probability distributions of each individual cluster might reduce some of these systematics (see Section 7.4).

The spatial distributions of young and old clusters highlight the effect of spiral arms (Figure 7). As illustrated by Figure 8, a spatial plot of the subsample of clusters with assigned ages younger than  $10^7$  yr clearly shows the spiral pattern and highlights the recent star formation in the nuclear region. The spiral pattern, as traced by the clusters, starts fading away for clusters older than approximately 300 Myr, and the (only) 64 clusters with ages older than  $10^9$  yr are consistent with a uniform distribution throughout the disk. As selection effects may differ in crowded and reddened areas of the field, these uncorrected spatial distributions should be taken with caution.

In summary, the age distribution of clusters younger than  $10^9$  yr and with masses  $\log(M/M_{\odot}) > 3.5$  is approximately a power law with an index of  $-1.0 \pm 0.2$ . While this is similar to previous results, the distribution is now defined with better age resolution (0.4 versus 0.7 dex), and it is based on more appropriate modeling than previous determinations when masses below  $\log(M/M_{\odot})$  of 4.5 are included.

## 6.2. Cluster Masses

The marginal distribution of all the cluster masses of the sample (i.e., the distribution summed over all ages and extinctions) is shown in Figure 9. It can be approximated by a power law with index  $-2.15 \pm 0.14$  for masses higher than

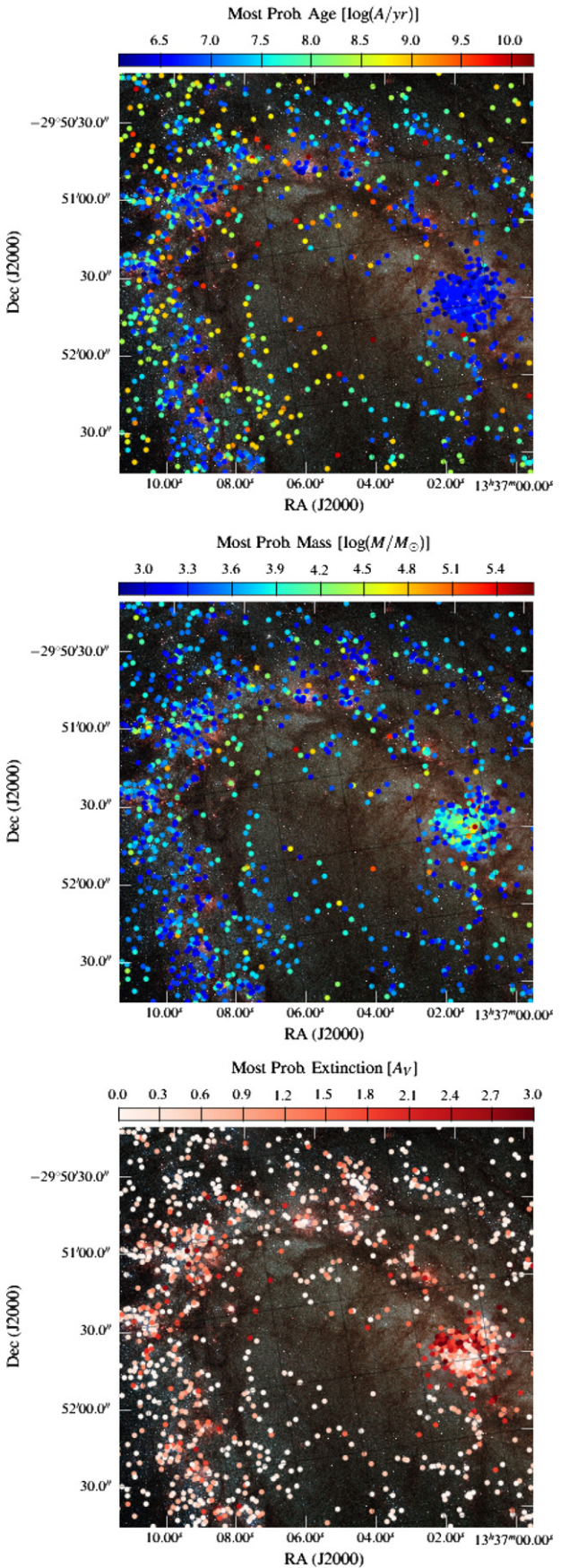


**Figure 7.** From top to bottom, recovered ages, masses, and extinctions vs. location in the galaxy. Colors are coded according to the respective scale and parameter given on the top of each figure.

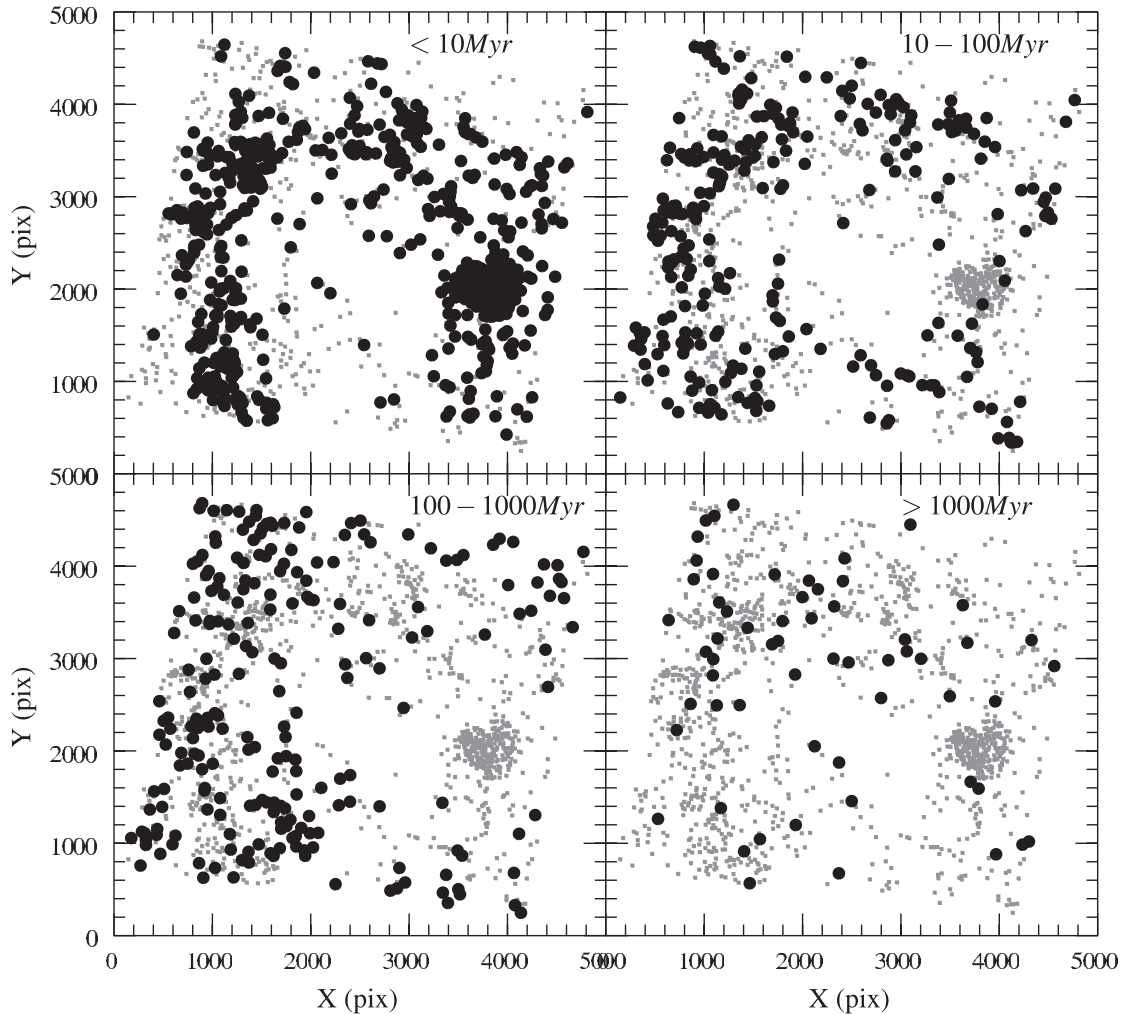


**Figure 8.** This figure represents the spatial age distribution of the cluster sample. On each panel, gray dots show the whole sample while black dots are objects with ages indicated in the top right corner.

$\log(M/M_\odot)$  of 3.5. The slope remains within the uncertainties ( $-2.09 \pm 0.13$ ) when we restrict the sample to clusters with ages between  $10^7$  and  $10^9$  yr. This confirms results from previous analyses, which also found approximatively power-law distributions (Anders et al. 2007; Dowell et al. 2008; Fall et al. 2009, 2005; Chandar et al. 2010; Bastian & de Mink 2009). Note that the power law of the prior mass distribution in our analysis is  $-1$ : the inversion is able to move away from the prior if necessary.

Below  $\log(M/M_\odot) = 3.5$  the derived mass distribution falls off, and ends with an apparent peak near  $\log(M/M_\odot) = 3$ . The peak at these low masses is unreliable, as it corresponds to the lower-mass limit of the collection of synthetic clusters used in the analysis: some of these objects may in fact be even less massive than  $10^3 M_\odot$ . The relative lack of clusters found between  $\log(M/M_\odot) = 3.2$  and 3.5 on the other hand is not related to any known artifact of the analysis (see, however, Section 7.4). It may well result from the incompleteness of the cluster sample at low fluxes: based on the Monte Carlo collection, we know that  $\log(M/M_\odot) = 3.7$  is the threshold mass under which more than half of the clusters have fluxes below the “completeness” limit (defined in Section 4) in at least one photometric passband.

Also, one should recall that (1) being faint, the low-mass objects have larger observational errors than massive ones,

and (2) having low masses while remaining above the detection limits these sources must be young, and therefore we are in the regime most sensitive to the modeling of H $\alpha$ .

In summary, the use of an approach that explicitly accounts for the stochastic nature of the observed clusters confirms a power-law behavior for the mass distribution of the M83 clusters, with an index of approximately  $-2.1 \pm 0.2$ , over the range of masses least affected by incompleteness, i.e., between  $\log(M/M_\odot) = 3.5$  and  $\log(M/M_\odot) = 5$ .

### 6.3. Nucleus versus Disk

The  $\sim 200$  star clusters of our sample that are part of the galaxy nucleus have derived ages younger than 10 Myr with our analysis ( $\sim 4$  Myr on average). This is not to say the nucleus contains no older objects, since most older clusters would remain undetected against the high background of the young sources. The higher average mass of the nuclear clusters ( $\sim 10^4 M_\odot$ ) is also compatible with the selection effects expected in an area crowded with bright objects.

Our main conclusions about the age distribution and the mass distribution of the M83 sample remain valid for the disk when the nuclear subsample is removed. The age distribution is changed only below 10 Myr, hence the fits shown in Figure 6 are essentially unaffected. The field clusters’ mass distribution is only slightly depleted at high masses compared to the mass

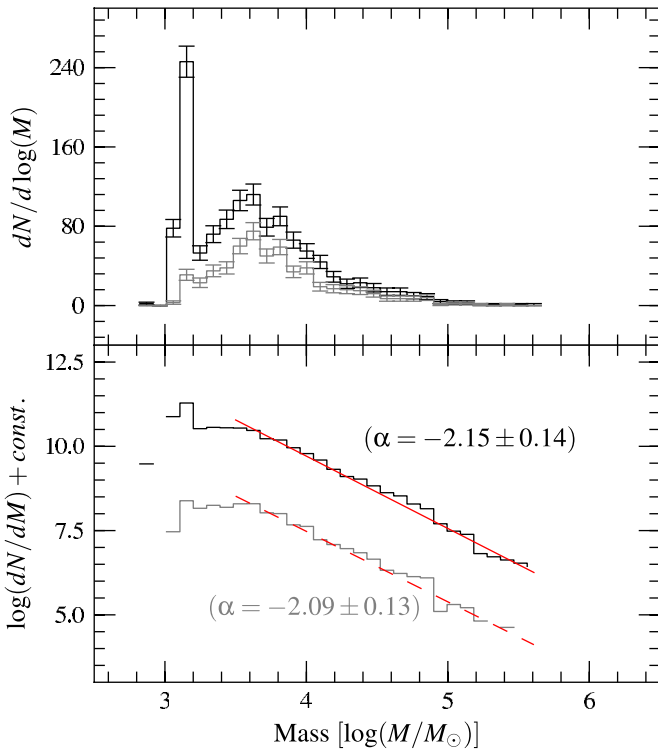


**Figure 9.** Mass distribution obtained with the stochastic analysis. This is the mass counterpart of the age distributions given in Figure 6. The black histograms represent the distribution for the whole set of identified objects whereas the gray ones only includes objects with estimated ages higher than 10 Myr. Error bars are the Poisson noise dispersions in each bin. Power-law fits are overlaid on top of the distributions (fitted masses are above  $10^{3.5} M_\odot$ ).

distribution of the whole sample, and this steepens the index of the fitted power law by only a few percent.

## 7. DISCUSSION

### 7.1. The Importance of the $H\alpha$ Filter, F657N

Despite the importance of  $H\alpha$  in the identification and age-dating of young clusters, this filter is still not used extensively. This is partly because extra difficulties come with these measurements and their interpretation. For example, the spatial extent of H II regions rarely matches that of the underlying optical continuum light leading to difficult aperture corrections, the escape fraction of ionizing photons is poorly known, the hot ionizing stars are a rare subpopulation and their number in any given cluster can deviate strongly from the expected mean (Cerviño et al. 2003). Considering these difficulties, we tested the results of the analysis of the M83 clusters with  $UBVI$  data alone, i.e., discarding the flux measurement in the  $H\alpha$  filter (F657N).

Figure 10 shows how the ages and masses estimated with  $H\alpha$  included (y-axis) compare with those obtained from  $UBVI$  alone (x-axis). In this figure, the colors represent changes in the estimate of the extinction parameter  $A_V$  between the two studies. The age-extinction degeneracy is apparent: younger ages come with naturally bluer colors on average, which can be compensated with a higher  $A_V$ . The blue dots show that without the narrowband filter information many clusters with  $H\alpha$  emission are given intermediate ages (40%). The masses of the corresponding clusters are systematically lowered when the  $H\alpha$  filter is included: the extra extinction required to match the colors at the now younger ages does not quite compensate for fading (younger clusters are intrinsically brighter for a given mass). The

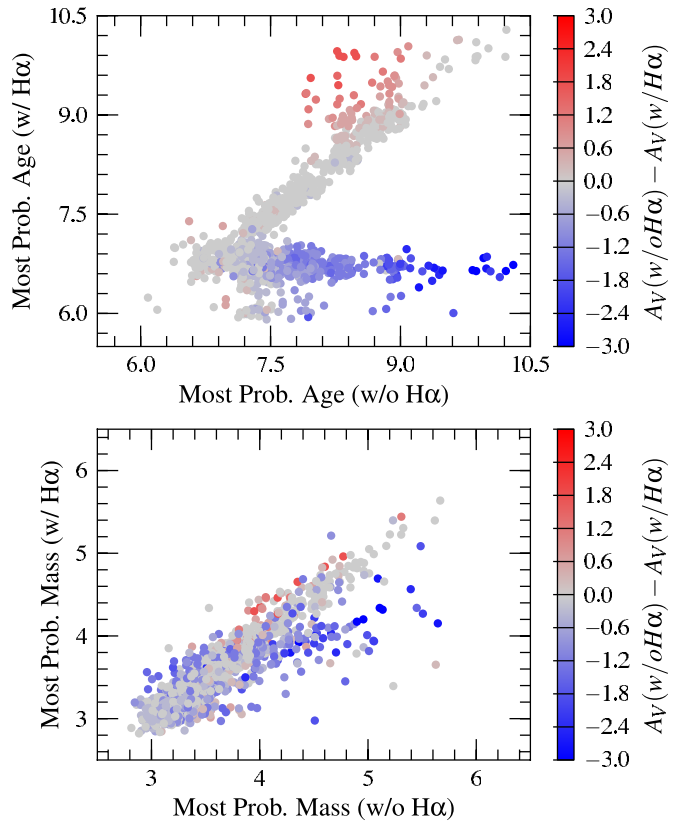


**Figure 10.** Comparing age and mass estimates (from the stochastic approach) based on  $UBVI+H\alpha$  (y-axes) and  $UBVI$  only (x-axes). Each dot represents the estimates of a star cluster color-coded according to the change in the extinction estimate (resulting from the inclusion of  $H\alpha$ ). Age estimates are compared in the top panel, while mass estimates are compared in the bottom panel. Projected age and mass distributions are represented in Figure 11.

red dots also illustrate the importance of the  $R$ -band information. Indeed when there is no  $H\alpha$  emission, the F657N filter becomes essentially a narrow  $R$ -band filter and acts as an extra constraint on the ages of clusters too old to contain ionizing stars.

Figure 11 presents the projected age and mass distributions. Clearly, the age distribution depends strongly on whether or not  $H\alpha$  narrowband (F657N) data are available. However, the effect on the mass distribution is limited: in particular, we conserve a similar power-law index. This suggests that the mass distribution of the sample based on our probabilistic approach is determined robustly down to about  $\log(M/M_\odot) = 3.5$ .

The age distributions with and without F657N differ, but which one is closer to reality? How sensitive are the young ages to details in the modeling or errors in the measurements? A color-color diagram involving F657N helps answering this question (Figure 12). The locus of the cloud of data points is extremely well represented by the collection of stochastic models with the extra degree of freedom provided by the reddening vector (this is reflected in the very good best- $\chi^2$  values obtained with the stochastic models). As opposed to the continuous models, the stochastic ones reproduce the “corner” of the observed distribution at  $(V-I) \simeq 0$  and  $(H\alpha - V) \simeq 0$ .

Errors would have to be unrealistically large and systematic to avoid an interpretation of Figure 12 with a large fraction of objects younger than 10 Myr. Changing the escape fraction of ionizing photons in the models would modify only the extent and color of the “plume” of young models in the figure. Changing the slope of the upper stellar IMF, the exact ages for which

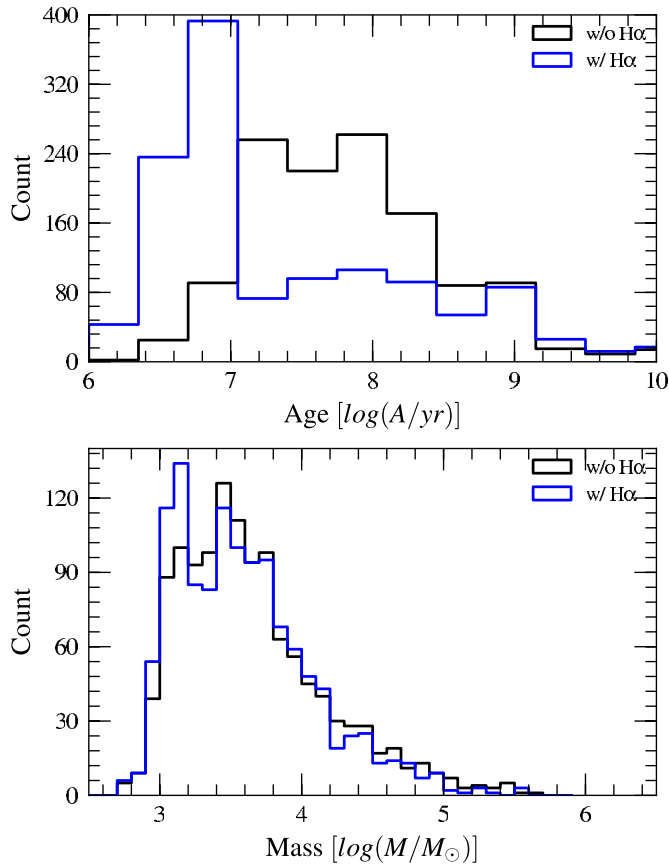


**Figure 11.** Comparing age and mass distributions (from the stochastic approach) based on  $UBV\text{H}\alpha$  (solid) and  $UBVI$  only (dotted). Age estimates are compared in the top panel, while mass estimates are compared in the bottom one.

models are computed, or the prior age and mass distributions of the model collection, would change how models are distributed along this plume and near the blue “hook” in the distribution. The slope of the extinction vector determines where exactly the dereddening line of a cluster reaches the cloud of models, but none of these changes would affect the fraction of young clusters greatly.

To summarize, the conclusion that about 55% of the clusters in the sample are less than  $10^7$  yr old is robust. On the other hand, individual ages below  $10^7$  yr are sensitive to model details.

## 7.2. Comparison with the Results based on Continuous Models

For a direct comparison, we have repeated the analysis of the M83 clusters with the traditional approach, based on the mean fluxes predicted by continuous models. The population synthesis assumptions are those of PÉGASE as described above, and the  $\chi^2$  calculation used to measure the quality of a fit is defined using fluxes as in the stochastic context (see Fouesneau & Lançon 2010, who present such a comparison for synthetic clusters).

The two-dimensional (2D) age–mass distribution resulting from the “continuous” analysis is shown in Figure 13. When compared to the results of the stochastic analysis (top panel of Figure 5), it shows a less homogeneous distribution in age. Fouesneau & Lançon (2010) explained why this is expected.

The “continuous” marginal distributions of cluster masses and cluster ages are compared to the stochastic ones in Figure 14. As already stated in the previous section, we consider the

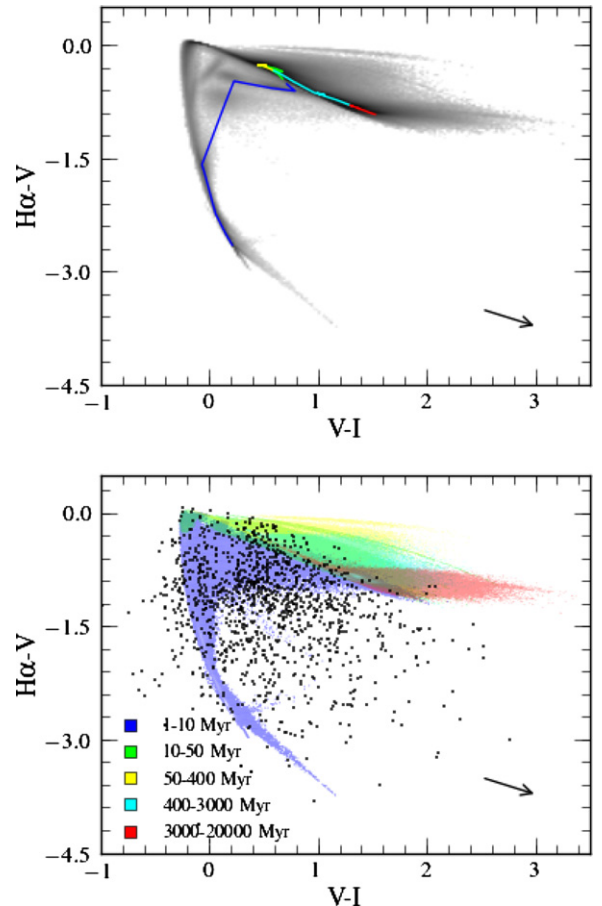


**Figure 12.** Models and M83 cluster data in a color–color plane that highlight the role of F657N. The model distribution is shown as a 2D histogram in the top panel, with the line of *continuous* models overlaid. The models are shown as colored contour maps in the bottom panel, together with the M83 data.

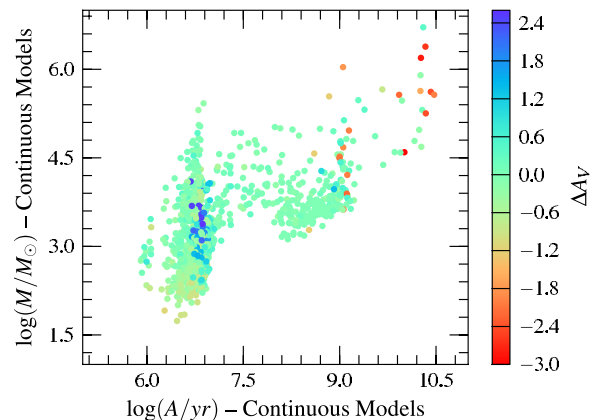


**Figure 13.** Age–mass distribution obtained from a  $\chi^2$ -fit using continuous models. Colors other than cyan and green highlight clusters for which the ages have changed most strongly between the continuous and the stochastic analysis (actually the scale is set by the corresponding change in  $A_V$ ).

flatness of the “stochastic” age distribution between  $10^7$  and  $10^9$  yr (in logarithmic bins) a robust result, while the dip in the “continuous” age distribution around  $5 \times 10^7$  yr and the excessive accumulation of very young clusters are artifacts of that method.

To first order, the mass distributions in the bottom right panel of Figure 14 are alike. Above  $\log(M/M_\odot) = 4$ , they are within

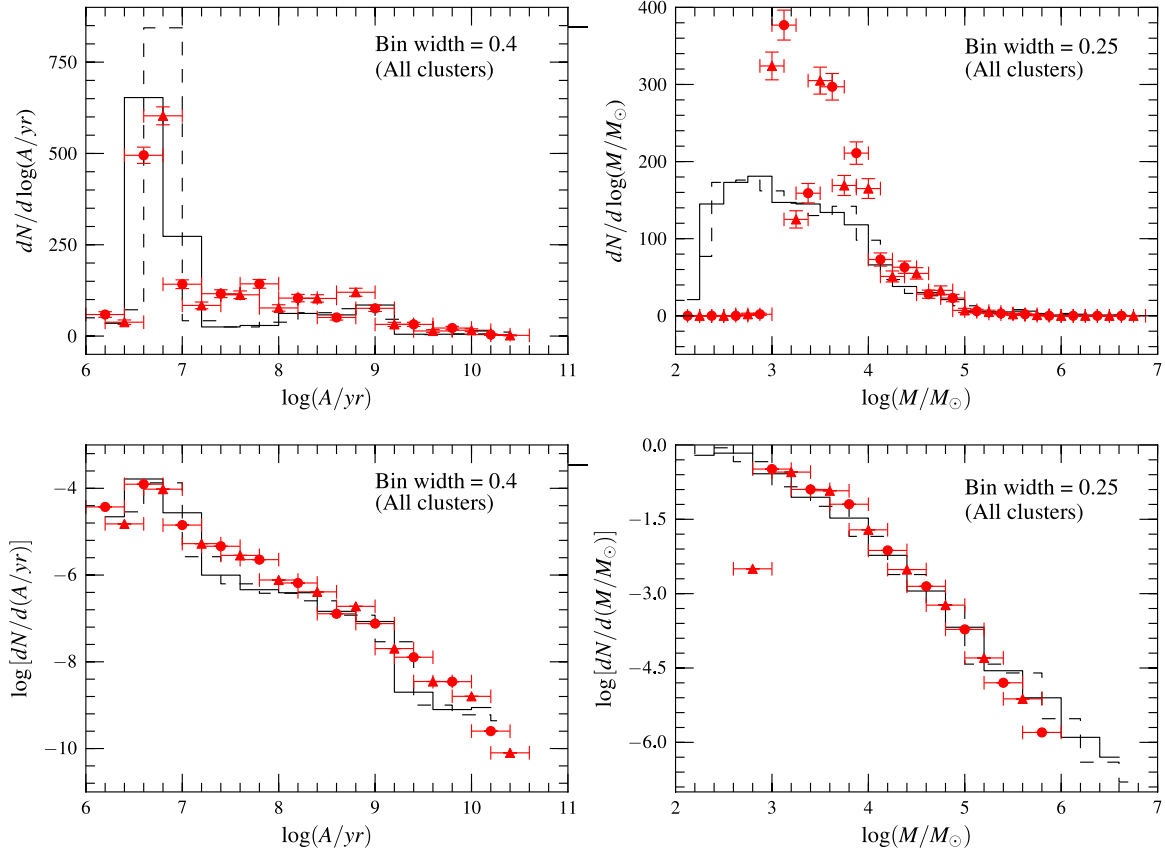


**Figure 14.** Marginal distributions of cluster ages and masses as obtained with continuous models (solid and dashed histograms) and with stochastic models (filled circle and triangle histogram levels). In each case, the histograms are shown for two sets of bin centers, offset from each other by half a bin size. To guide the eye, error bars representing Poisson standard deviations are shown in the top panels.

(A color version of this figure is available in the online journal.)

$2\sigma$  of each other ( $\sigma$  representing Poisson standard deviations in the bins).

A closer look shows that the analysis with continuous models leads to a subset of very young and low-mass clusters ( $\log(M/M_\odot) < 3$ ) that are not found with the “stochastic” analysis. At first glance, one may think that this difference simply reflects a bias of the “stochastic” analysis, due to the lower-mass limit of the model collection ( $10^3 M_\odot$ ). In fact, it is due at least in part to a known issue of the analysis of finite clusters with continuous models (Fouesneau & Lançon 2010, their Figure 9). A purposely designed test was run with the WFC3 filters of the M83 observations. The analysis of synthetic clusters, all more massive than  $10^3 M_\odot$  and brighter than the magnitude limits of the M83 observations, shows that  $\sim 35\%$  of the clusters with actual  $\log(M/M_\odot)$  between 3.2 and 3.7 are assigned masses below  $\log(M/M_\odot) = 3$  when analyzed with continuous models. In the upper right panel of Figure 14, we see that the difference between the distributions derived with stochastic and continuous models for  $3.2 < \log(M/M_\odot) < 3.7$  represents just about  $\sim 35\%$  of all the clusters in that mass range.

More details on the differences between the stochastic and the continuous analysis are given in Appendix A. In particular, the one-by-one comparison of the “continuous” and the “stochastic” ages and masses are shown. Individual ages differ by more than 0.3 dex for 28% of the sample.

A comparison between the “continuous” results found in the present study (i.e., based on PÉGASE models analog to the stochastic models) and those of Chandar et al. (2010) is provided

in Appendix B. Using different population synthesis models changes the ages of 25% of the clusters by more than 0.3 dex, but in a way that does not modify global results.

### 7.3. Comparison with Morphological or Spectroscopic Ages

Age estimates based on methods other than the analysis of the broad- and narrowband spectral energy distributions (SED) are available for small subsets of the star clusters of our sample. Unfortunately, these subsets do not extend to the lowest cluster masses.

Whitmore et al. (2011) have devised a purely morphological classification scheme for star clusters based on images in several photometric passbands, including  $H\alpha$ . The categories are chosen such as to represent subsequent phases of the morphological evolution of a typical cluster, and the classification sequence is therefore expected to correlate with age. Their Figure 3 shows that the morphological category indeed relates to the SED ages estimated using traditional models with a continuously populated IMF.

Figure 15 focuses on the 64 star clusters of Whitmore et al. (2011) for which the morphological classification is considered most robust. Eight of the 64 clusters are located in the nucleus, 56 in the field. The bottom panel compares our age estimates with the photometric ages obtained by Whitmore et al. (2011) based on continuous models. Both of these age estimates use  $UBVI+H\alpha$  photometry. The two sets of photometric ages agree well, except for a scarcely populated horizontal branch

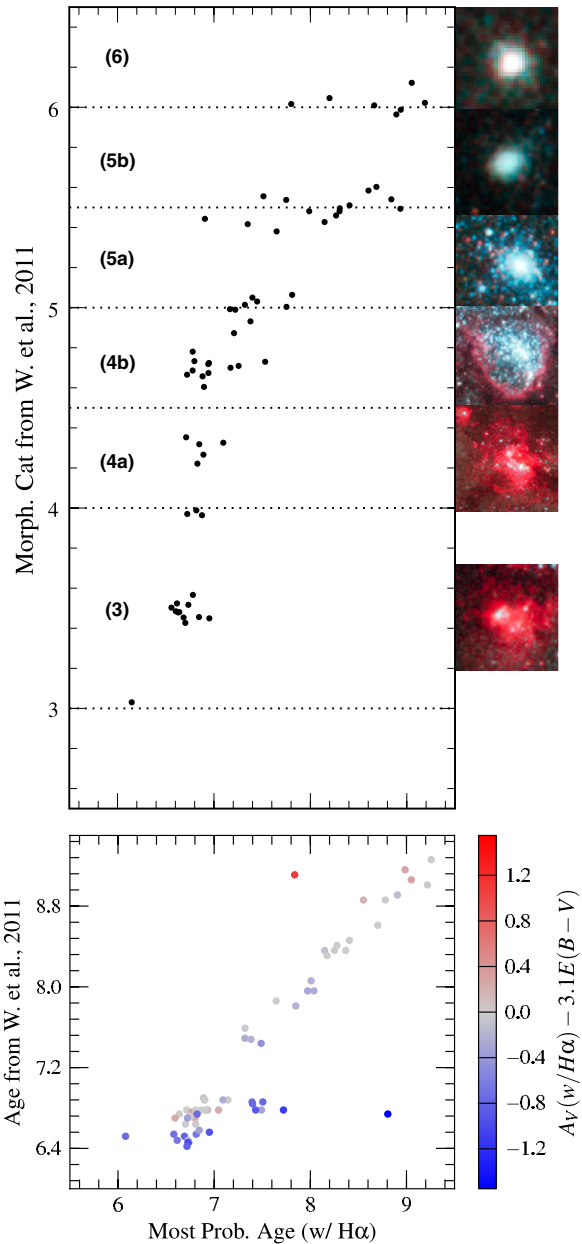


**Figure 15.** Ages derived from the approach detailed in this paper [x-axis] compared to the  $H\alpha$  morphology categories from Whitmore et al. (2011) (top) and to ages from traditional models (bottom), for the clusters in common. Boxes on the top panel refer to statistics on the morphological categories presented in the cited paper.

of “catastrophic differences” around  $\log(A/\text{yr}) = 6.9$  from Whitmore et al. (2011) (only 10% of the sample) and an associated gap in the one-to-one relation around  $\log(A/\text{yr}) = 7.2$ , a behavior rather typical for this sort of plot (Fouesneau & Lançon 2010). The deviant clusters are in the morphological categories 5a and 5b according to Whitmore et al. (2011), i.e., they are unlikely to be as young as the photometric analysis with continuous models suggest.

The top panel of Figure 15 shows the relationship between photometric age and morphological category obtained with the new photometric age estimates, i.e., those based on stochastic models. The clusters that are outliers in the upper panel were also outliers in the version of this figure given by Whitmore et al. (2011): they formed a vertical extension of young photometric ages into older morphological categories. But for one object, this

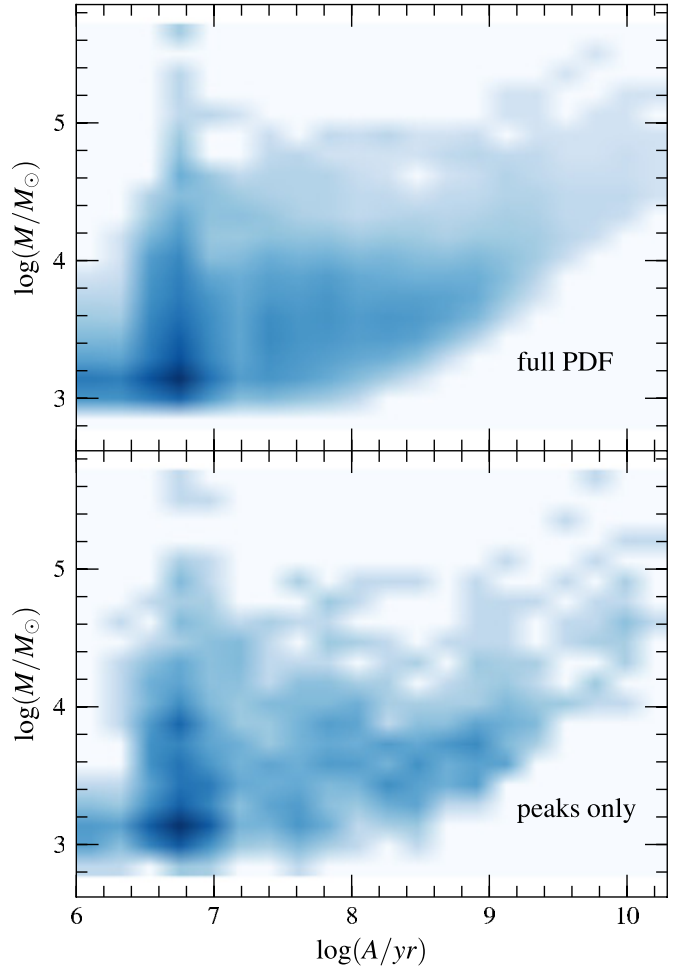


**Figure 16.** Age–mass distributions obtained for the M83 sample from the probabilistic analysis. Top: distribution obtained by summing the individual posterior probability maps of the clusters (i.e., the *extended* method). Bottom: density map obtained from the most probable age and mass values shown in the top panel of Figure 5 (i.e., the *peak* method, for which each point is replaced by a patch to produce a density representation).

vertical extension has now disappeared. As a result, the average photometric ages of categories 5a and 5b shift to older values by about 0.1 dex. This remains within the error bars associated with the dispersion within the categories. All in all, the figure remains similar to its original version.

Spectroscopic age estimates are available for 13 luminous clusters in the nuclear region from Wofford et al. (2011). These were obtained using Space Telescope Imaging Spectrograph FUV spectra covering the range from 1200 to 1700 Å (e.g., including the strong N V and C IV lines as well as several other weaker lines). Wofford et al. (2011) fit the observations using both semiempirical models, based on a library of Galactic O and B stars observed with *IUE*, and theoretical Starburst 99 models (Leitherer & Chen 2009, continuously sampled IMF). They find ages between 2 and 5 Myr for nine clusters and ages between 10 and 20 Myr for four. The photometric ages quoted in that article, based on the same five photometric passbands as in our paper and on the method of Chandar et al. (2010), are in good agreement with the spectroscopic ages except for one of the four objects with spectroscopic ages above 10 Myr (see Wofford et al. 2011, Table 3). Our analysis with stochastic models returns ages between 3 and 9 Myr for all the 13 clusters. These ages are within 0.2 dex of the spectroscopic results except for the three oldest objects of Wofford et al. (2011). The differences for these

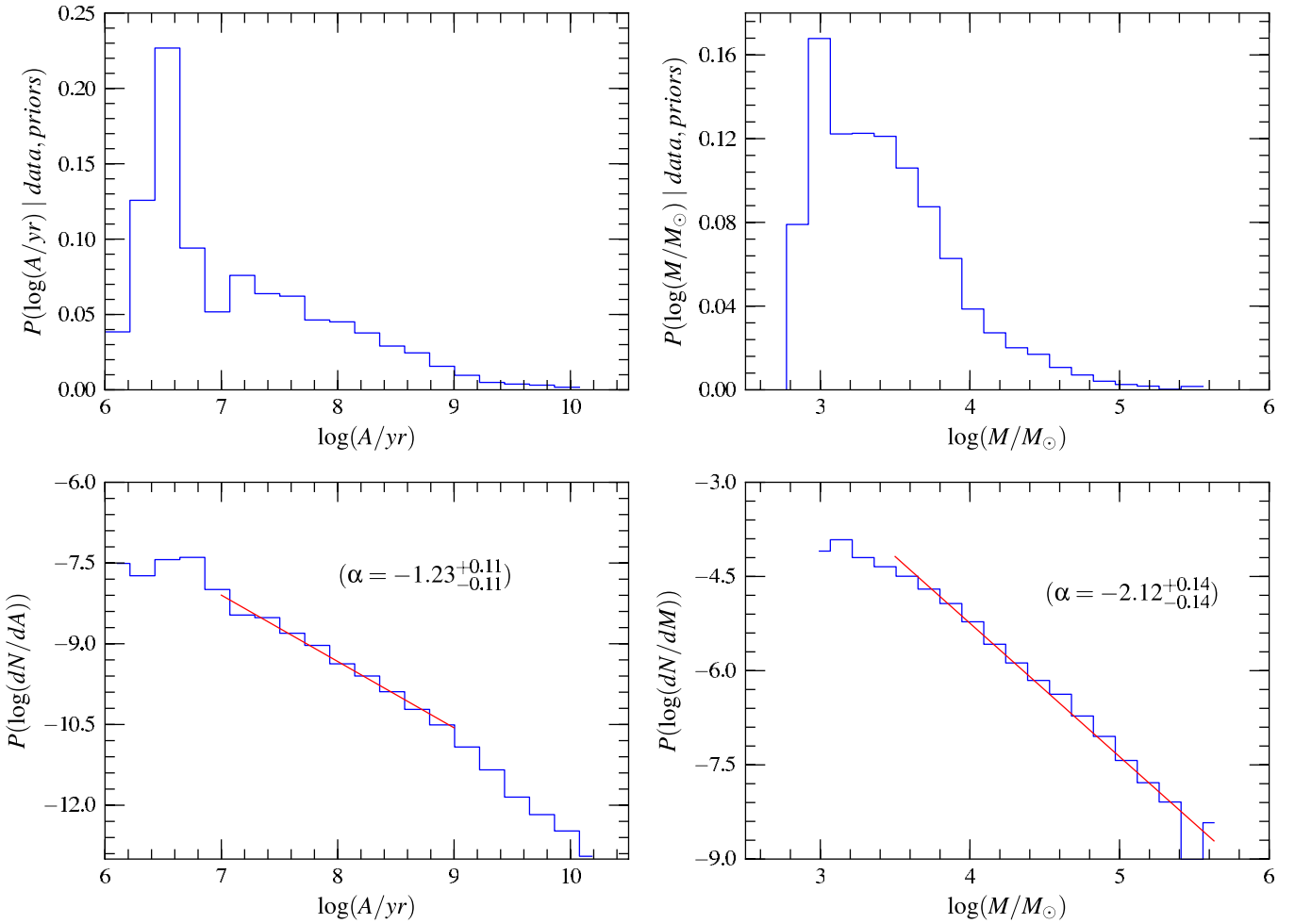


**Figure 17.** Age and mass distributions obtained with the approach explored in Section 7.4. Left: age distribution, for comparison with Figure 6. Right: mass distribution, for comparison with Figure 9.

(A color version of this figure is available in the online journal.)

three objects are due to differing assumptions in the population synthesis codes rather than to stochastic modeling. Indeed, when we use models with a continuously sampled IMF, we obtain ages within 0.1 dex of those derived in the stochastic context, as long as both are based on the same synthesis parameters (e.g., those defined in Section 3). This comparison is meaningful because the three clusters are massive (masses in the range of  $5 \times 10^4$ – $1 \times 10^6 M_\odot$ , depending on the method used). All in all, the agreement between stochastic and non-stochastic ages is very satisfactory considering the diversity of approaches.

#### 7.4. Toward a More Complete Usage of Posterior Probability Distributions

The main aim of this paper is the comparison of results of traditional analysis methods with results based on the method of Fouesneau & Lançon (2010), for a sample of real clusters in M83. Following these authors, we have chosen the peak of the posterior probability distribution to assign an age, a mass, and an extinction value to each cluster. This method can be extended to use the full posterior probability distribution for each cluster rather than the peak approximation. In this section, we explore this approach by comparing the results of this *extended* method with those of the *peak* method for our cluster sample in M83.

A complete theoretical study of the extended method in various observational regimes deserves a separate paper.

The three-dimensional probability distributions of age, mass, and extinction obtained for the 1242 individual clusters of our sample are quite complex and display a variety of patterns. We have found about a dozen typical behaviors, that depend on the region of color-luminosity space the clusters are in, as well as on observational error bars. It is difficult to find a satisfactory way of translating this complexity into simple error bars on the estimates provided by the “peak” method. As already described in Fouesneau & Lançon (2010), the main trends are set by the age–mass and age–extinction degeneracies, which define directions along which probability peaks tend to be elongated. Within this gross picture other patterns are seen. For instance, it is relatively common to find bimodal distributions with one peak at young ages ( $< 10^7$  yr) and one at intermediate ages ( $\sim 10^9$  yr). The relative strengths of these peaks depend on the error bars on the  $H\alpha$  measurement. This particular pattern can be understood with the discussion we provide in Appendix A concerning the left panel of Figure 19.

A new estimate of the age and mass distributions of the cluster sample as a whole was obtained by summing the age–mass probability distribution of individual clusters (marginalized over extinction). With this approach, uncertainties on the estimated parameters and any covariance between them are automatically

accounted for. The sensitivity to binning choices is reduced. The resulting map is shown in Figure 16. For convenience, the figure also recalls the results of the “peak” method (Figure 5) as a directly comparable density map. The global structure with both approaches is similar. For instance, both methods obtain an overdensity of young, low-mass objects. Overall, by accounting for the entire posterior probability distributions instead of only the location of their maxima we smear out local variations in the derived age–mass map.

The one-dimensional age and mass distributions obtained with the extended approach are presented in Figure 17, and can be compared to those shown in Figures 6 and 9. The masses of the cluster sample are found to follow a power law with an index of  $-2.1$  for  $\log(M/M_{\odot}) > 3.5$ , a result essentially identical to the one we obtained with the peak method. The restriction to ages older than 10 Myr does not change the index value significantly. The dip seen near  $\log(M/M_{\odot}) = 3.3$  with the peak method has been smoothed into a more robust plateau. The age distribution in Figure 17 has a somewhat steeper power law ( $\alpha = -1.23$ ) than found previously ( $-1.08$ ). Its restriction to masses greater than  $\log(M/M_{\odot}) = 3.5$  reduces the absolute value of the age power-law index by some 10%. The slopes of the age distributions, as derived with either the extended or the peak method, remain within the formal  $1\sigma$  confidence interval of each other for this sample.

In summary, the age–mass distributions found for our sample of M83 clusters are similar whether we use the extended method or the peak method. Spurious small-scale features in the result of the peak method tend to disappear with the extended method. The extended method deserves further investigation in the future.

## 8. CONCLUSIONS

Most star clusters in nearby galaxies have masses below  $10^5 M_{\odot}$ , and hence their integrated fluxes and colors can be strongly affected by stochastic fluctuations in the number of massive stars (strictly post-main-sequence stars). Fouesneau & Lançon (2010) previously introduced new stochastically sampled stellar population model predictions, and developed a probabilistic method for estimating the ages, extinctions, and masses of star clusters from these models. The models were tested using synthetic clusters. For the purpose of the present paper, we enhanced the stochastic models by including predictions for narrowband filters and extending the Monte Carlo collection of synthetic clusters to include higher cluster masses. We compared the predictions from the stochastically sampled models with observations of a sample of real star clusters. Our observations consist of integrated  $UBVIH\alpha$  fluxes of star clusters in the nearby spiral galaxy M83, which was observed with the WFC3 on the *HST*. This is the same catalog of clusters analyzed by Chandar et al. (2010) using predictions from more traditional models which assume a “continuously sampled” stellar IMF.

The locus of the collection of stochastic models in color space (e.g., Figure 2) shows excellent agreement with that of the collection of cluster observations. Clusters with broadband colors either bluer or redder than those of the traditional models find a natural match in the stochastic model collection, in which some synthetic clusters have underpopulated or overpopulated red post-main-sequence branches. Similarly, the locus of stochastic models in color–color planes that include  $H\alpha$  fluxes (e.g., Figure 12), and hence take into account the random character

of the number of ionizing stars in a cluster, provide a natural match with the observations.

A key result of the study is the importance of including a narrowband filter measurement in the analysis, which to date has been used in relatively few works. A comparison of age and mass estimates with and without the  $H\alpha$  filter shows that 30% of the sources have age estimates that change by more than 0.3 dex in age in our analysis (factor of two). The errors are systematic: without the narrowband measurement, many young clusters are not recognized as such.

The use of stochastic models has allowed us to derive the age–mass distribution of the star clusters in the M83 sample with a better resolution in time than was possible before, and we extend both age and mass distributions to lower masses (down to  $\log(M/M_{\odot}) \sim 3.3$ ). Above  $\log(M/M_{\odot}) = 3.7$ , the mass limit at which completeness issues in the sample become severe, the mass distribution derived from the analysis with stochastic models closely resembles the distribution obtained with traditional models in previous work. More specifically, the overall slope of the mass distribution remains within the range of values indicated by Chandar et al. (2010), i.e., power law of index near  $-2$ . The age distribution is now free of the dip between  $10^7$  and  $5 \times 10^7$  yr that was a known artifact of the analysis of clusters subject to stochastic fluctuations with continuous models. Overall, we confirm that it declines more-or-less continuously starting at young ages as already suggested by the results of Chandar et al. (2010). Between  $10^7$  and  $10^9$  yr, the data are consistent with a flat distribution in logarithmic age units, which corresponds to  $dN/dA \propto A^{-1}$ . The sample contains only a handful of clusters older than 1 Gyr because these are too faint for easy detection.

In this paper, we also begin the process of extending the analysis from a unique “most probable” value (corresponding to the peak in the posterior distribution, the *peak* approach) to a full probabilistic description of the correlated age, mass, and extinction properties of each individual clusters (i.e., the *extended* method). The extended method is expected to be more robust than the peak method. It does not lose any of the information carried by individual posterior probability distributions about uncertainties, about correlations between parameters, or about multiple (almost) equally probable solutions. The age–mass distributions obtained with the extended method for our M83 cluster sample remain similar to those obtained previously. Spurious substructure seen in *peak* method distributions when plotted with narrow bins disappears. We plan to test the extended method more systematically in various observational regimes in the future.

It may seem surprising at first glance that low-resolution age and mass distributions of cluster samples are not modified more radically by the move from a traditional analysis to a method based on explicitly stochastic models. Changing a power-law slope radically, with data that extends over about 2 dex in age and mass, requires strong and systematic changes, but the changes induced by the switch from traditional models to stochastic models are not of this nature. Fouesneau & Lançon (2010) had predicted that overall mass distributions would be rather insensitive to this switch, and we have confirmed this with the M83 sample. Their figures also indicated that changes in the age assignments due to the switch to stochastic models would mostly affect subsets of objects in particular ranges of age and mass (i.e., the high-resolution features of the age distribution), instead of changing the global balance between young, intermediate, and old objects. This is also what we found for the M83 sample in

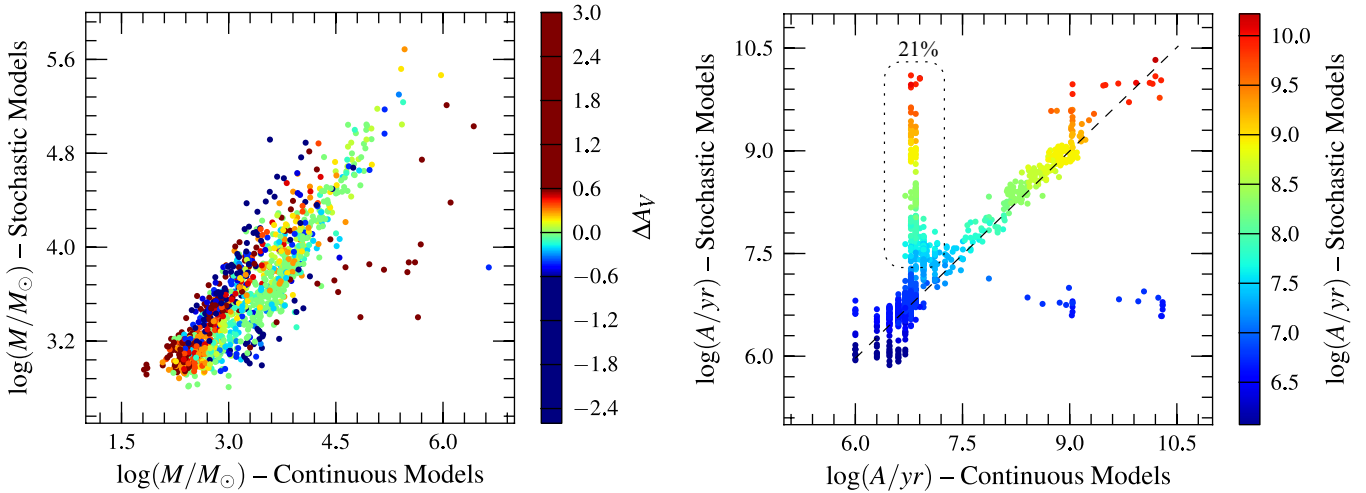


**Figure 18.** Comparison of the ages and masses obtained when analyzing the M83 cluster sample with “continuous” models on one hand and with “stochastic” models on the other. The dashed line highlights the one-to-one relation, and the dotted box the vertical sequence mentioned in the text.

the present paper: the  $-1 (\pm 0.2)$  slope of the best-fit power law to the age distribution is a robust result for the sample.

As we push to lower masses and larger samples of fainter clusters, the improved accuracy and time resolution achievable with the new stochastic methods allows us to address new questions, such as local variations among cluster populations within individual galaxies. For instance, we find that the subsample of young clusters in our data set clearly displays the spiral structure of M83, while this structure progressively disappears in samples older than a few hundred millions of years. The cluster age–mass distribution in the field we have studied is thus (not surprisingly) partly determined by the location of this field with respect to the spiral arms. This level of details can now be taken into account when comparing galaxies or areas within galaxies.

This paper is based on observations taken with the NASA/ESA *Hubble Space Telescope* obtained at the Space Telescope Science Institute, which is operated by AURA, Inc., under NASA contract NAS5-26555. It uses Early Release Science observations made by WFC3 Science Oversight Committee. The analysis of the results made extensive usage of the Topcat software, available under General Public Licence from <http://www.starlink.ac.uk/topcat/>.

We thank the anonymous referee for their careful reading and suggestions which improved our manuscript.

## APPENDIX A

### MORE DETAILS ON THE COMPARISON BETWEEN THE CONTINUOUS AND THE STOCHASTIC ANALYSIS

This appendix provides some additional details about the comparison described in Section 7.2.

In Figure 18, we provide the direct cluster-by-cluster comparison between the ages and masses derived on one hand from an analysis with *stochastic* models, on the other hand from the best- $\chi^2$  fit to *continuous* models (both based on the population synthesis code PÉGASE, and on *UBVI* and *Hα* photometry). It is essential to note that in this section (as in most of the paper), the parameters we assign in the stochastic context are *not* those of the single Monte Carlo model that provides the best- $\chi^2$  fit, but those that maximize the posterior probability distribution of the cluster observations. 72% of the clusters have ages within 0.3 dex of each other, while 28% have ages more than 0.3 dex

apart. For the clusters with similar ages in both approaches, the residuals have a bell-shaped distribution with an FWHM of 0.3 dex. Most of the clusters with highly method-dependent ages lie on a vertical sequence in the second panel of Figure 18 (21% of all clusters; see the box on the figure). They are assigned young ages with continuous models, while the analysis based on stochastic models leads to a range of older ages. The young ages of the continuous analysis come with high values of the extinction parameter (because young cluster models are intrinsically blue) and low masses (because young cluster models are intrinsically bright), while the older ages of the stochastic analysis are associated with low extinction parameters, and masses that are typically 0.8 dex higher. This is seen in the first panel of the figure as a one-sided broadening of the one-to-one relation toward higher “stochastic” masses (dark blue symbols). Because this happens at all masses, the consequence for the mass distribution is a slight offset in  $\log(M/M_\odot)$  with hardly any change in the slope of a fitted power law. The consequence for the age distribution is a change in the strength of the peak of young clusters ( $< 10^7$  yr), and a redistribution of these clusters over other ages in a way that again has little effect on the slope of a fitted power law. Note that for comparison with other work in the literature one also has to keep in mind differences in the population synthesis assumptions of various authors (see, e.g., Appendix B).

The remainder of this appendix is provided for readers particularly interested in the subtleties of the behavior of our analysis with stochastic models. It gives further insight into the roles played by the prior distributions of cluster ages and masses, and by the observational error bars.

Color–color and color–magnitude plots can be used to understand the origin of the vertical sequence in the age diagram just described. For brevity we will call these particular clusters the “deviant clusters” in this paragraph. We looked at many color combinations and confirmed that the deviant clusters are located in a region of broadband color space where young reddened models and old models overlap. The projection we found most useful for this discussion is  $(H\alpha - V)$  versus  $(V - I)$ . The deviant clusters are highlighted in this diagram in the first panel of Figure 19, which must be compared to Figure 12. About one half of the deviant clusters (shown in blue and cyan) lie along the line where most of the old- and intermediate-age synthetic clusters congregate, near the upper envelope of the total cluster

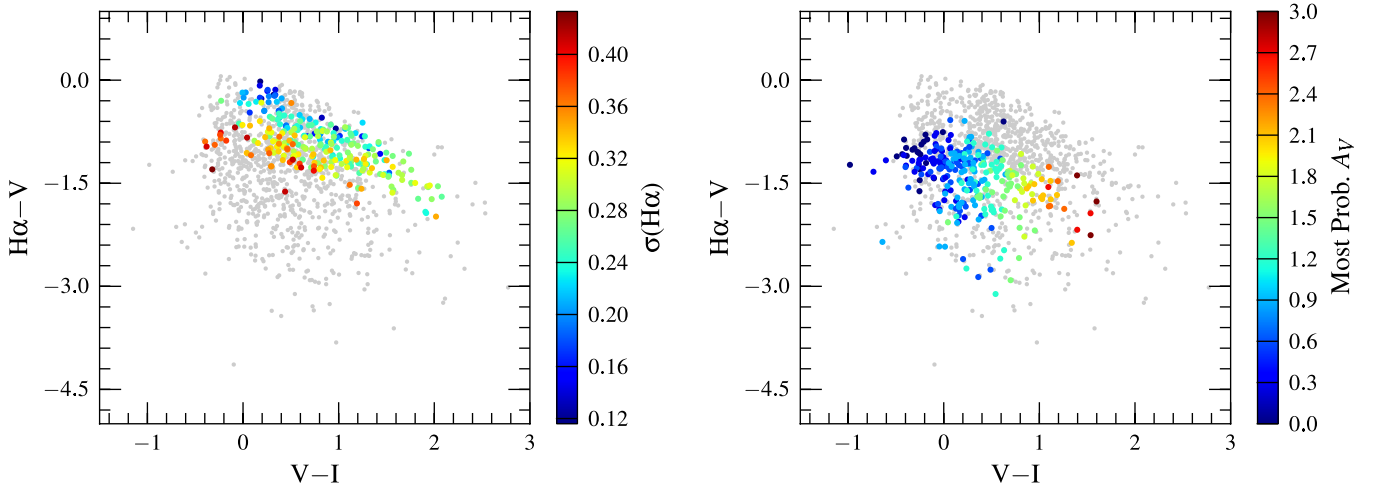


**Figure 19.** Color–color plots similar to Figure 12, but with specific objects highlighted. In the first panel, the colored symbols identify the clusters that populate the main vertical structure of the second panel of Figure 18 (i.e., the “deviant clusters”). The color code shows the observational uncertainty on the clusters’  $H\alpha$  measurement (in magnitudes). In the second panel, the colored symbols highlight low-mass clusters whose ages are similar in the stochastic and in the continuous contexts, but whose masses differ. Here the color code shows the associated  $A_V$ . Both subsets are discussed in the text.

sample in this diagram. The fact that they are assigned intermediate and old ages in the stochastic analysis is an immediate consequence of the high density of intermediate and old model clusters in that area. The fact that some are assigned very young ages in the continuous analysis appears as a consequence of the “single best-fit” approach of that continuous analysis: by chance the model closest to them happens to be a young one, but a small shift in the observed colors (well within the photometric error bars) could change the derived age significantly since young reddened models and older dust-free ones are found side by side. The second half of the deviant clusters (shown in yellow and red) are located in a region where only young reddened model clusters exist. These objects however *all* have errors larger than 0.25 mag on the F657N measurement (and the errors increase for deviant clusters located further away from the upper envelope of the data points). For these clusters we see the effects of the observational errors clearly. The multi-dimensional  $2\sigma$  error boxes around each of them reach well into the above-mentioned region of color–color space where the density of intermediate age and old clusters is high. Models outside such an error box contribute negligibly to the posterior probability distribution, but all models inside may contribute significantly (Bayes’ theorem). Because the error boxes contain overwhelmingly more intermediate and old models than young reddened models, our analysis favors the older solution. For clusters at the same location in color–color space but with much smaller error bars on  $H\alpha$ , young ages are returned. Note that the number of clusters concerned by this discussion is too small to change any of the main results discussed in this paper.

A second more subtle effect contributes to the one-sided broadening of the mass versus mass plot, this time only in the regime of small masses ( $\log(M/M_\odot) < 3.5$  in the continuous analysis—red symbols in the first panel of Figure 18). These objects have identical ages with the continuous and with the stochastic analysis (frequently within 0.1 dex), but the “stochastic” masses are larger than the “continuous” masses by 0.3–0.6 dex. Their location in the most useful color–color diagram is highlighted in the second panel of Figure 19. We see in Figure 12 that the vast majority of the young stochastic cluster models lie *not* along the line of models with a continuously sampled IMF, but rather on a curved

“plume” at bluer colors. This would be the case for any prior mass distributions that has more low-mass clusters than high-mass clusters. As a consequence, the analysis of the posterior probability distribution favors the models in this bluer “plume” and assigns a correspondingly larger extinction. The age changes little when compared to the analysis with a continuously sampled IMF, but the larger extinction must be compensated for with a somewhat larger mass. This effect concerns about 20% of the clusters. It has a noticeable effect on the mass distribution derived from stochastic models only below  $\log(M/M_\odot) = 3.6$ .

## APPENDIX B COMPARISON WITH THE AGES AND MASSES OF CHANDAR ET AL. (2010)

Chandar et al. (2010) use continuous population synthesis models. Figure 10 of their article shows the age–mass distributions they obtain when assuming solar and twice solar metallicity. They are qualitatively very similar to the distribution shown here in Figure 13.

The differences are due in part to the underlying population synthesis assumptions, in part to the analysis method. Chandar et al. (2010) use models from Bruzual & Charlot (2003) with a Chabrier IMF, and they account for hydrogen line emission with an escape fraction of 0.4 (the value that, in their analysis, provides best-fit qualities on average). The fit for age and extinction is done using magnitudes, and the mass is then determined from the  $V$ -band absolute magnitude. As a consequence of using magnitudes in their case, fluxes in our case, the different photometric bands are given different weights in both studies, and the reduced  $\chi^2$  values cannot be compared directly (except very grossly: in both cases a  $\chi^2$  value above a few indicates a poor fit).

Figure 20 directly compares ages retrieved by Chandar et al. (2010) and ages we obtain in this present paper. Ages are similar for 85% of the clusters (and for 95% of the clusters with small observational errors). These objects are on a curved line that deviates slightly from the one-to-one diagonal, so that strictly speaking only 75% of all the clusters have ages that agree to within 0.3 dex with both methods. Differences one could call “catastrophic” occur for 15% of the

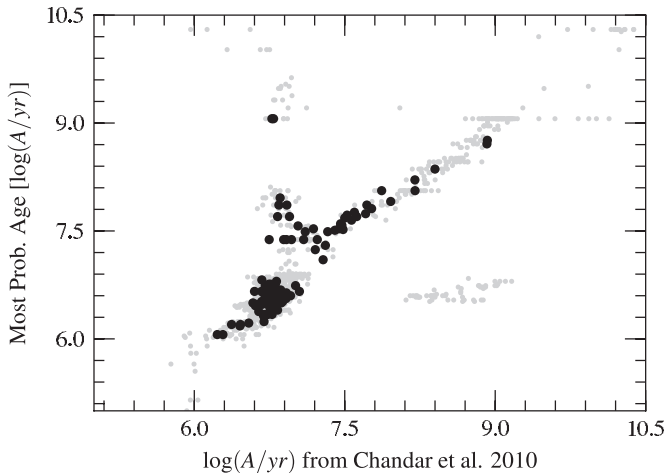


**Figure 20.** Ages derived from with *continuous* models by Chandar et al. (2010) [x-axis] and in this paper [y-axis]. Large black dots highlight the 114 clusters for which the error in all filters are smaller than 0.13 mag.

clusters, and are not restricted to observations with large error bars. These differences depend rather sensitively on the way nebular emission is accounted for in the models (the vertical branch of “catastrophic errors” disappears and the horizontal one gains clusters when we remove the nebular emission from the continuous models used here). They also depend on the range over which the extinction parameter is allowed to vary.

## REFERENCES

- Anders, P., Bissantz, N., Boysen, L., de Grijs, R., & Fritze-v. Alvensleben, U. 2007, *MNRAS*, **377**, 91
- Barbaro, C., & Bertelli, C. 1977, *A&A*, **54**, 243
- Bastian, N., Adamo, A., Gieles, M., et al. 2011, *MNRAS*, **417**, L6
- Bastian, N., & de Mink, S. E. 2009, *MNRAS*, **398**, L11
- Billett, O. H., Hunter, D. A., & Elmegreen, B. G. 2002, *AJ*, **123**, 1454
- Bohlin, R. C. 2007, in ASP Conf. Ser. 364, The Future of Photometric Spectrophotometric and Polarimetric Standardization, ed. C. Sterken (San Francisco, CA: ASP), 315
- Bressan, A., Fagotto, F., Bertelli, G., & Chiosi, C. 1993, *A&AS*, **100**, 647
- Bruzual, G. 2002, in IAU Symp. 207, Extragalactic Star Clusters, ed. D. P. Geisler, E. K. Grebel, & D. Minniti (Cambridge: Cambridge Univ. Press), 616
- Bruzual, G., & Charlot, S. 2003, *MNRAS*, **344**, 1000
- Cardelli, J. A., Clayton, G. C., & Mathis, J. S. 1989, *ApJ*, **345**, 245
- Cerviño, M., & Luridiana, V. 2006, *A&A*, **451**, 475
- Cerviño, M., Luridiana, V., Pérez, E., Vilchez, J. M., & Valls-Gabaud, D. 2003, *A&A*, **407**, 177
- Chandar, R., Whitmore, B. C., Kim, H., et al. 2010, *ApJ*, **719**, 966
- Converse, J. M., & Stahler, S. W. 2011, *MNRAS*, **410**, 2787
- de Grijs, R. 2009, *Ap&SS*, **324**, 283
- Deveikis, V., Narbutis, D., Stonkutė, R., Bridžius, A., & Vansevičius, V. 2008, *Balt. Astron.*, **17**, 351
- Dowell, J. D., Buckalew, B. A., & Tan, J. C. 2008, *AJ*, **135**, 823
- Elmegreen, B. G., & Hunter, D. A. 2010, *ApJ*, **712**, 604
- Fall, S. M., Chandar, R., & Whitmore, B. C. 2005, *ApJ*, **631**, L133
- Fall, S. M., Chandar, R., & Whitmore, B. C. 2009, *ApJ*, **704**, 453
- Fioc, M., & Rocca-Volmerange, B. 1997, *A&A*, **326**, 950
- Fouesneau, M., & Lançon, A. 2010, *A&A*, **521**, A22
- Gil de Paz, A., Boissier, S., Madore, B. F., et al. 2007, *ApJS*, **173**, 185
- Girardi, L., & Bica, E. 1993, *A&A*, **274**, 279
- Groenewegen, M. A. T., & de Jong, T. 1993, *A&A*, **267**, 410
- Hunter, D. A., Elmegreen, B. G., Dupuy, T. J., & Mortonson, M. 2003, *AJ*, **126**, 1836
- Johnson, L. C., Seth, A. C., Dalcanton, J. J., et al. 2011, in Proc. Stellar Clusters and Associations: A RIA Workshop on Gaia, ed. E. J. Alfaro Navarro, A. T. Gallego Calvente, & M. R. Zapatero Osorio, 129 (<http://sca.iaa.es/content/proceedings>)
- Kroupa, P., & Boily, C. M. 2002, *MNRAS*, **336**, 1188
- Kroupa, P., Tout, C. A., & Gilmore, G. 1993, *MNRAS*, **262**, 545
- Lamers, H. J. G. L. M., Gieles, M., & Portegies Zwart, S. F. 2005, *A&A*, **429**, 173
- Lançon, A., & Mouhcine, M. 2000, in ASP Conf. Ser. 211, Massive Stellar Clusters, ed. A. Lançon & C. M. Boily (San Francisco, CA: ASP), 34
- Larsen, S. S. 2009, *A&A*, **494**, 539
- Larsen, S. S., & Richtler, T. 2000, *A&A*, **354**, 836
- Leitherer, C., & Chen, J. 2009, *New Astron.*, **14**, 356
- Lejeune, T., Cuisinier, F., & Buser, R. 1997, *A&AS*, **125**, 229
- Maíz Apellániz, J. 2009, *Ap&SS*, **324**, 95
- Parmentier, G., & de Grijs, R. 2008, *MNRAS*, **383**, 1103
- Piskunov, A. E., Kharchenko, N. V., Schilbach, E., et al. 2009, *A&A*, **507**, L5
- Popescu, B., & Hanson, M. M. 2010, *ApJ*, **724**, 296
- Schlegel, D. J., Finkbeiner, D. P., & Davis, M. 1998, *ApJ*, **500**, 525
- Searle, L., Wilkinson, A., & Bagnuolo, W. G. 1980, *ApJ*, **239**, 803
- Thim, F., Tammann, G. A., Saha, A., et al. 2003, *ApJ*, **590**, 256
- Whitmore, B. C., Chandar, R., & Fall, S. M. 2007, *AJ*, **133**, 1067
- Whitmore, B. C., Chandar, R., Kim, H., et al. 2011, *ApJ*, **729**, 78
- Whitmore, B. C., & Zhang, Q. 2002, *AJ*, **124**, 1418
- Wofford, A., Leitherer, C., & Chandar, R. 2011, *ApJ*, **727**, 100